Title: Cholinergic Modulation Shifts the Response of CA1 Pyramidal Cells to Depolarizing Ramps via TRPM4 Channels with Potential Implications for Place Field Firing

Abbreviated Title: Cholinergic Modulation Shifts the Response of CA1 Pyramidal Cells

Author Names and Affiliations: Crescent Combe[1], Carol Upchurch[2], Carmen C. Canavier[2]* and Sonia Gasparini[1,2]*

[1]Neuroscience Center of Excellence, and [2]Department of Cell Biology and Anatomy, School of Medicine, Louisiana State University Health Sciences Center, New Orleans, Louisiana, USA 70112

* these authors jointly supervised this work

Corresponding author: Sonia Gasparini, Neuroscience Center, Louisiana State University Health Sciences Center, New Orleans, 2020 Gravier St., New Orleans, LA 70112, sgaspa1@lsuhsc.edu

Number of pages: 41

Number of figures: 11 (+ 3 supplemental figures)

Conflict of interest statement: The authors declare no competing financial interests.

Acknowledgements: This work was funded by NIH R01 MH115832 under the CRCNS program to SG and CCC and by the Research Enhancement Program of the School of Medicine at the Louisiana State University Health Sciences Center to SG. The simulations utilized resources provided by NSF 2018936. We would like to thank Drs. Christopher Del Negro, Barbara Ehrlich and Dan Johnston for helpful discussions.

Abstract

A synergistic combination of *in vitro* electrophysiology and multicompartmental modeling of rat CA1 pyramidal neurons identified TRPM4 channels as major drivers of cholinergic modulation of the firing rate during a triangular current ramp, which emulates the bump in synaptic input received while traversing the place field. In control, fewer spikes at lower frequencies are elicited on the down-ramp compared to the up-ramp due to long-term inactivation of the Na_V channel. The cholinergic agonist carbachol (CCh) removes or even reverses this spike rate adaptation, causing more spikes to be elicited on the down-ramp than the up-ramp. CCh application during Schaffer collateral stimulation designed to simulate a ramp produces similar shifts in the center of mass of firing to later in the ramp. The non-specific TRP antagonist flufenamic acid and the TRPM4-specific blockers CBA and 9-phenanthrol, but not the TRPC-specific antagonist SKF96365, reverse the effect of CCh; this implicates the Ca^{2+}-activated nonspecific cation current, I_{CAN}, carried by TRPM4 channels. The cholinergic shift of the center of mass of firing is prevented by strong intracellular Ca^{2+} buffering but not by antagonists for IP_3 and ryanodine receptors, ruling out a role for known mechanisms of release from intracellular Ca^{2+} stores. Pharmacology combined with modeling suggest that $[Ca^{2+}]$ in a nanodomain near the TRPM4 channel is elevated through an unknown source that requires both muscarinic receptor activation and depolarization-induced Ca^{2+} influx during the ramp. Activation of the regenerative inward TRPM4 current in the model qualitatively replicates and provides putative underlying mechanisms for the experimental observations.

Introduction

Release of the neuromodulator acetylcholine is thought to be correlated with certain brain states or functions (Pepeu and Giovannini, 2004). In the hippocampal formation, elevated acetylcholine is associated with exploration (Bianchi et al., 2003), particular memory processes (Micheau and Marighetto, 2011), REM sleep (Hutchison and Rathore, 2015), and response to novelty (Acquas et al., 1996; Thiel et al., 1998; Giovannini et al., 2001).

The major cholinergic input to the hippocampus is from the medial septum and diagonal band of Broca, which innervate all hippocampal subfields (Dutar et al., 1995). As for the degree to which acetylcholine release is spatially targeted, this is still under debate (Disney and Higley, 2020; Sarter and Lustig, 2020); however it has been shown that CA1 receives cholinergic afferents in all layers, although at different densities (Nyakas et al., 1987; Aznavour et al., 2002). Pyramidal neurons express G-protein-coupled metabotropic muscarinic acetylcholine receptors (mAChRs) (Levey et al., 1995), more so than they do ionotropic (nicotinic) receptors, which are primarily on interneurons in this region (Dani and Bertrand, 2007). M_1 mAChRs, in particular, are found on both dendritic shafts and spines of CA1 pyramidal neurons (Yamasaki et al., 2010).

Elevated acetylcholine in the hippocampal formation is thought to favor memory encoding, and modulates theta oscillations (Hasselmo, 2006), which in turn modulate place cell firing (Easton et al., 2012). There is evidence that cholinergic activity regulates long-term synaptic plasticity (Huerta and Lisman, 1995; Palacios-Filardo and Mellor, 2019; Fernández de Sevilla et al., 2021). Cholinergic activation also influences intrinsic properties of neurons, which result in membrane potential depolarization (Brown and Adams, 1980), increase in firing rate (Benardo and Prince, 1982), and modulation of input/output relationships, for example switching from burst to regular firing (Azouz et al., 1994).

In addition to suppressing several potassium currents (Brown and Adams, 1980; Hoffman and Johnston, 1998; Buchanan et al., 2010; Giessel and Sabatini, 2010), cholinergic stimulation has been linked to the activation of a calcium-activated, non-specific cation current, I_{CAN} (Colino and Halliwell, 1993; Egorov et al., 2002; Yoshida et al., 2012). I_{CAN} is attributed to current flowing through channels of the transient receptor potential (TRP) family (Guinamard et al., 2010; Reboreda et al., 2011). The canonical TRP channel, TRPC, has been implicated in cholinergic-mediated persistent firing ((Zhang et al., 2011; Arboit et al., 2020), but see (Egorov et al., 2019)). There is indirect evidence, however, of involvement of TRPM4 channels in the cholinergic activation of I_{CAN}. TRPM4 channel activation downstream of group I metabotropic glutamate receptors in pre-Botzinger cells (Mironov, 2008), implicates the $G_{q/11}$ pathway shared by $mGluR_{1/5}$ and mAChR $M_{1/3/5}$. Although TRPM4 channels are known to be expressed in the soma and apical dendrites of CA1 pyramidal dendrites (Riquelme et al., 2021), their known functions in these neurons are currently limited to a minor role in the afterdepolarization following action potential trains (Lei et al., 2014) and involvement in NMDA-mediated LTP (Menigoz et al., 2016).

Previously, we found that when triangular shaped current ramps intended to emulate the depolarizing input received by a place cell during a place field traversal (Epsztein et al., 2011) were injected at the soma or dendrites of CA1 pyramidal neurons, they elicited fewer spikes on the down-ramp than on the up-ramp (Upchurch et al., 2022). In the current study, we investigated the effect of cholinergic modulation on this firing pattern *in vitro* (slice electrophysiology) and *in silico* (multi-compartmental NEURON model). We found that, at comparable maximum firing rates, cholinergic activation shifts the center of mass of firing to the latter half of the ramp, both for current injection ramps as well as for synaptically-driven depolarizations. Both CCh and sustained depolarization are required to produce the rightward shift in the center of mass of firing along the ramp. This shift is blocked by antagonists specific for TRPM4 channels or by intracellular Ca^{2+} buffering, but not by IP_3 or ryanodine receptor antagonists. The TRPM4 channels have a micromolar half-activation concentration of Ca^{2+} (Nilius et al., 2004), which implies that a restricted Ca^{2+} nanodomain near the channel mouth is required to elicit substantial opening of TRPM4 channels. Thus, whatever the Ca^{2+} source that activates the TRPM4 channels, it is likely co-localized with them.

Results

Asymmetric firing on symmetric ramps is modulated by cholinergic activation

We have previously used 2 and 10 second long triangular-shaped current ramps (Upchurch et al., 2022) to emulate the depolarizing input received by a place cell during a place field traversal (Epsztein et al., 2011); the amplitude of the ramps was adjusted for each cell to produce peak frequencies between 10 and 25 Hz, as observed in place cells *in vivo* (Hargreaves et al., 2007; Resnik et al., 2012; Bittner et al., 2015). Regardless of whether these ramps are injected at the soma or in the dendrites of CA1 pyramidal neurons, they elicit fewer spikes on the down-ramp than on the up-ramp, due to adaptation mediated by long-term sodium channel inactivation (Fernandez and White, 2010; Venkatesan et al., 2014; Upchurch et al., 2022). Place cell firing is modulated by experience such that the center of mass of the place field shifts in a direction opposite the direction of motion as the environment becomes more familiar (Mehta et al., 2000). This modulation is strongest when animals are first introduced to a novel environment (Roth et al., 2012), suggesting involvement of a novelty signal. Since elevated acetylcholine is thought to be such a signal (Acquas et al., 1996; Giovannini et al., 2001), we investigated the effect of cholinergic neuromodulation on this firing rate adaptation (Figure 1).

Figure 1A1 and 1E1 show typical voltage responses to two-second-long symmetric ramps injected in the soma or dendrites (approximately 200 μm from soma) under control conditions. This type of response results in a positive value for the normalized difference between spikes fired on the up-ramp versus the down-ramp (we call this an adaptation index, see Methods for definition). A positive index means that neurons fire more on the up-ramp than the down-ramp, whereas a negative value indicates the converse,

112 and is therefore a good metric to determine shifts in the center of mass of the firing of CA1 pyramidal
113 neurons in different conditions. In some trials, under control conditions we applied a baseline depolarization
114 prior to the ramp, in order to capture the variability observed *in vivo* (Harvey et al., 2009; Epsztein et al.,
115 2011). Application of the cholinergic agonist carbachol (CCh, 2 μM) caused a depolarization of 2-6 mV.
116 We compensated for this depolarization by injecting tonic hyperpolarizing current to reestablish the original
117 membrane potential (see also (Losonczy et al., 2008)), as indicated by an offset from the 0 pA current level
118 in the traces of the injected current ramps. The amplitude of background fluctuations in the resting
119 membrane potential increased from a few tenths of a mV in control to 2-4 mV in CCh. Moreover, the
120 threshold for action potential generation became more hyperpolarized. For all these reasons, we were not
121 able to consistently vary the membrane potential using baseline depolarizations in the presence of CCh,
122 because baseline depolarization alone frequently evoked spiking. As a result of the increased excitability
123 in CCh, smaller current ramps were sufficient to produce the same peak frequencies as in control (note
124 the difference in the injected ramp currents below the voltage trace in Figures 1A1 vs. 1B1 and 1E1 vs.
125 1F1). Under these conditions, CCh caused a shift of the center of mass of firing to later in the ramp (Figure
126 1B1 and 1F1), which resulted in a decreased value of the adaptation index which became negative for
127 most cells, as shown in the scatter plot of group data (Figure 1D and 1H). The shift is evident in the plots
128 of the frequency as a function of time (compare Figure 1A2 vs. 1B2 and 1E2 vs. 1F2). As in (Mainen and
129 Sejnowski, 1995), the raster plots of the spike times were characterized by variability in the timing of action
130 potentials among different trials in the same neuron (Figures 1A3, 1B3 and 1E3, 1F3). However, the
131 variability appears to be independent of the amount of current injected, as demonstrated by trials that are
132 grouped as a function of the injected peak current amplitude. Moreover, the raster plots show how the
133 center of mass of firing overall shifted from early in the ramp in control conditions to later in the ramp in the
134 presence of carbachol. This shift was significant for short (2 s) ramps in the soma (control 0.33 ± 0.02,
135 CCh -0.25 ± 0.03; $t(20) = 16.741$; $p < 0.0005$; $n = 21$), long (10 s) ramps in the soma (control 0.24 ± 0.02,
136 CCh -0.33 ± 0.06; $t(18) = 9.854$; $p < 0.0005$; $n = 19$), as well as for short and long ramps in the dendrites
137 (2 s ramps: control 0.49 ± 0.04, CCh -0.45 ± 0.07; $t(18) = 12.529$; $p < 0.0005$; $n = 19$; 10 s ramps: control
138 0.37 ± 0.02, CCh -0.16 ± 0.06; $t(9) = 10.582$; $p < 0.0005$; $n = 10$).

139 Plots of instantaneous frequency versus current injection are shown in Figure 1C1, 1C2, 1G1 and 1G2.
140 These plots provide a way to assess firing rate adaptation or acceleration when the injected current is not
141 a square pulse (Venugopal et al., 2015). In control (Figure 1C1 and 1G1), frequencies were higher on the
142 up-ramp (filled circles) and decreased on the down-ramp (open circles) at similar values of injected current.
143 This hysteretic clockwise motion corresponds to spike rate adaptation, in which the firing rate decreases
144 at a constant value of injected current. In contrast, in the presence of CCh, the motion was variable; it
145 could be essentially linear as shown in the somatic example in Figure 1C2 or even counter-clockwise as
146 in the dendritic example in Figure 1G2. The frequency/current (f/I) plots in Figure 1 – supplement 1 show
147 the clockwise hysteresis in control and different cases of reversal or removal of adaptation in the presence

148 of CCh for somatic recordings, with panels A and B showing acceleration, and panels C and D showing
149 linearization. A linear motion indicates no hysteresis, although often the neurons fire at lower current
150 injections on the down-ramp (defined as sustained linear in (Venugopal et al., 2015)), whereas counter-
151 clockwise motion corresponds to an acceleration of the firing rate that would be observed during injection
152 of a constant current. Both of these variants correspond to an effective removal of the spike rate adaptation
153 by cholinergic activation. These results also demonstrate that cholinergic activity shifts the center of mass
154 of firing to later times during a symmetric ramp. We speculate that the level of cholinergic modulation could
155 therefore be a source of rapid modification of the timing of place cell firing relative to position in the place
156 field. Our summary results in Figure 1 show that carbachol similarly affects 2 s and 10 s ramps, and we
157 present only the data for the 2 second ramps for subsequent figures.

158 Since the initial membrane potential and the amount of current injected could potentially affect the center
159 of mass of firing, confounding the effects of cholinergic modulation, we plotted the adaptation index as a
160 function of the initial membrane potential (Figure 1 – figure supplement 2A) and of injected current
161 amplitude (Figure 1 - figure supplement 2B), in control conditions and in the presence of carbachol (2 μM)
162 for each trial for all recorded neurons, both for somatic and dendritic recordings. Likewise, since the input
163 resistance of the neuron could potentially skew the center of mass of firing, we plotted the average
164 adaptation index as a function of the steady-state input resistance in control conditions and in the presence
165 of carbachol for each somatic and dendritic recording (Figure 1 - figure supplement 2C). In all cases, it is
166 apparent that the main factor determining the adaptation index, and therefore whether the center of mass
167 of firing occurs earlier or later in the ramp, is the presence or absence of carbachol rather than initial
168 membrane potential, current injection amplitude, or input resistance.

169 The later onset of spiking in CCh in the experiments described above may be attributable to the smaller
170 current ramps, but the persistence of spiking without adaptation is striking in comparison to control. The
171 use of smaller ramps to achieve similar firing rates may be justified by analogy with the presynaptic action
172 of ACh to reduce glutamate release (Hasselmo, 2006). Since the current injection protocols described
173 above only account for the effects of cholinergic agonists on the postsynaptic neuron, we examined the
174 effects of carbachol on synaptically-driven membrane potential ramps, where pre- and postsynaptic effects
175 can be probed at the same time. To this end, we stimulated the Schaffer collateral fibers with bipolar
176 electrodes and recorded the responses from the somata of CA1 pyramidal neurons (Figure 2). The
177 electrical stimulation consisted of 30 stimuli for a total duration of ~2 s. The stimulation pattern was adjusted
178 according to a linear, symmetric ramp as in (Hsu et al., 2018), such that the frequency increased and
179 decreased symmetrically, starting at 6.7 Hz and peaking in the middle of the ramp at 25 Hz, the target
180 peak frequency in the current injection experiments. The intensity of stimulation was adjusted such that
181 neurons would fire in response to 40-65% of the total inputs under control conditions, and was kept
182 constant in control conditions and in the presence of carbachol. In both conditions, firing was more frequent

183 in the middle of the ramp, because of the higher stimulation frequency. However, as in the current injection
184 protocols in Figure 1, some variability was observed in the timing of the spikes across trials, as can be
185 appreciated in the raster plots. In control conditions, the neurons tended to fire more in the first half of the
186 ramp (Figure 2A), whereas in the presence of carbachol they tended to fire more on the second half of the
187 ramp (Figure 2B). The adaptation index was calculated in a similar manner as in Figure 1, as the
188 normalized difference between the number of spikes in the first and the second half of the ramp. On
189 average, the adaptation index decreased from 0.18 ± 0.03 in control to -0.17 ± 0.04 in the presence of
190 carbachol, $t(10) = 6.873$, $p < 0.0005$, $n = 11$ (Figure 2C). This shift was partly due to a decrease in the
191 amplitude of the EPSPs (Figure 2D); the average amplitude of the first EPSP in control (8.83 ± 0.82 mV)
192 was significantly larger than the average first EPSP in CCh (6.81 ± 0.52 mV; $t(10) = 4.127$; $p = 0.002$; $n =$
193 11). In addition, the decay of the EPSPs appeared to slow down later in the ramp in the presence of CCh
194 (compare EPSPs indicated by diamonds in the two conditions), resulting in an increase in temporal
195 summation and excitability. These results show that carbachol tends to shift the center of mass of firing to
196 later in the ramp in the case of a synaptically-driven depolarization as well as in response to a ramp of
197 injected current.

198 Carbachol is often used to more easily study cholinergic signaling in biological tissues, because it is not
199 susceptible to hydrolysis by acetylcholinesterase, which is preserved and active in hippocampal slices
200 (Avignone and Cherubini, 1999). To verify that the effects of the endogenous neuromodulator were
201 comparable to those of its synthetic analog, we repeated the experiments in Figure 1 with different
202 concentrations of acetylcholine. In this and all following sets of experiments, the amplitude of current
203 injection was adjusted for each cell and condition to produce peak frequencies between 10 and 25 Hz as
204 described above. Acetylcholine caused a depolarization of the V_m in a dose-dependent manner. As before,
205 we compensated for this depolarization by injecting hyperpolarizing current to restore the initial V_m (Figure
206 3). Like carbachol, acetylcholine shifted the center of mass of firing to later in the ramp, albeit to a more
207 moderate degree (Figure 3A-D). A one-way repeated measures ANOVA was carried out to determine if
208 there was an effect on the adaptation index of three concentrations of ACh within the same neurons. The
209 assumption of sphericity was violated, so a Greenhouse-Geisser correction was applied ($\varepsilon = 0.574$). There
210 was a significant effect of ACh on the adaptation index, plotted in Figure 3E (control 0.35 ± 0.04; 2 μM ACh
211 0.14 ± 0.04; 10 μM ACh 0.00 ± 0.06; 15 μM ACh -0.02 ± 0.06; $F(1.722, 20.665) = 44.360$; $p < 0.0005$, $n =$
212 13). Bonferroni-adjusted post hoc tests demonstrated significant differences between the control condition
213 and all concentrations of ACh (all comparisons $p < 0.0005$), and between the lowest concentration and the
214 subsequent higher concentrations (for 2 μM compared to 10 μM, $p = 0.001$; for 2 μM compared to 15 μM,
215 $p = 0.01$). There was not a significant difference between 10 μM and 15 μM ACh. Due to likely degradation
216 via acetylcholinesterase, we speculate that the actual concentration in the slices is lower than the applied
217 one. CCh is not susceptible to degradation by acetylcholinesterase, and its concentration, which in our
218 experiments is markedly lower than that used in many studies on cholinergic modulation of neuronal

activity (Bland et al., 1988; Fisahn et al., 1998; Knauer et al., 2013), is therefore more consistent, which may explain the more pronounced shift in spiking in Figure 1 as compared to Figure 3. Nonetheless, our results with ACh suggest that there are concentration-dependent effects of the endogenous neuromodulator on firing rate adaptation. Fluctuations in ACh levels could therefore have implications for the firing of a place cell within its place field.

Cholinergic-associated shift in the timing of firing during the ramp is mediated by TRPM4 channels

An increase in firing on the down-ramp compared to the up-ramp induced by cholinergic activation could result from 1) a decrease in an outward current and/or 2) an increase in an inward current. The cascade of events that follow cholinergic activation in these neurons includes the suppression of a number of outward currents (Halliwell and Adams, 1982; Hoffman and Johnston, 1998; Buchanan et al., 2010; Giessel and Sabatini, 2010), some of which are also involved in firing rate adaptation (Stocker et al., 1999; Gu et al., 2005; Pedarzani et al., 2005; Otto et al., 2006; Chen et al., 2014). Although the SK channel clearly contributes to adaptation when the dendrites are stimulated at high frequency (>50 Hz) (Combe et al., 2018), we have previously examined the contribution of small-conductance calcium-activated potassium (SK) current, M-type potassium current, and A-type potassium current with respect to the asymmetric firing in response to symmetric current ramps (Upchurch et al., 2022). We found that, in the relatively low range of firing frequencies evoked by this type of stimulation, the adaptation induced by these K^+ currents (including SK) does not play a role in shifting action potentials to earlier times during the ramp. However, cholinergic activation has also been shown to activate a non-specific inward cationic current, I_{CAN}, that is thought to be carried by certain TRP channels (Guinamard et al., 2010; Reboreda et al., 2011). Flufenamic acid (FFA) has been shown to block a variety of TRP channels in hippocampal neurons (Partridge and Valenzuela, 2000) and elsewhere (Guinamard et al., 2013). After observing the typical response to CCh, responses to symmetric ramps were recorded while FFA (100 μM) was applied along with CCh (Figure 4A and 4B). FFA shifted most action potentials back to the up-ramp as shown in the examples in Figure 4A1-4A3 and 4B1-4B3, effectively reversing the shift triggered by CCh. The differences in adaptation index across the three conditions were found to be significantly different by repeated measures ANOVA in both somatic recordings (control 0.35 ± 0.05, CCh -0.36 ± 0.09, CCh+FFA 0.25 ± 0.06; $F(2,16) = 65.835$; $p < 0.0005$; $n = 9$; Figure 4A4) and dendritic recordings (control 0.52 ± 0.02, CCh -0.54 ± 0.11, CCh+FFA 0.20 ± 0.08; $F(2,16) = 60.680$; $p < 0.0005$; $n = 9$; Figure 4B4). Bonferroni-adjusted pairwise comparisons indicated that for somatic recordings, the differences were significantly different between control and CCh ($p < 0.0005$), and between CCh and CCh+FFA ($p < 0.0005$), but not between control and CCh+FFA ($p = 0.43$). For dendritic recordings, the differences were significantly different between control and CCh ($p < 0.0005$), CCh and CCh+FFA ($p < 0.0005$), and control and CCh+FFA ($p = 0.02$). In most cases, the adaptation index reverted to a positive value with the application of FFA from a negative value in CCh

alone, and in all cases was closer to the control value with FFA than with CCh alone. The failure of the adaptation index to return to control values in FFA may reflect an incomplete block of TRP channels or an additional effect of CCh. Overall, these data suggest that the shift in the center of mass of firing to later along the ramp that is associated with cholinergic activity is due, in large part, to activation of TRP channels.

The TRPC subfamily has been implicated as being responsible for I_{CAN} in some neurons and is thought to be activated by elements downstream of muscarinic acetylcholine receptor activation (Putney, 2005), which makes it an attractive candidate, mechanistically, for this cholinergic-mediated shift in action potential firing along the depolarizing ramp. Cholinergic stimulation of $G_{q/11}$-coupled mAChRs results in phospholipase C hydrolysis of membrane constituent phosphatidylinositol 4,5-bisphosphate (PIP_2) into inositol 1,4,5-trisphosphate (IP_3) and diacylglycerol (DAG). IP_3 stimulates IP_3 receptor (IP_3R) associated Ca^{2+} release from the endoplasmic reticulum, regulating TRPC channel activity via calmodulin (Zhu, 2005), while DAG activates TRPC channels directly (Hofmann et al., 1999; Mederos Y Schnitzler et al., 2018).

In a set of experiments similar to those above, the TRPC-specific antagonist SKF96365 (50 μM) was added after CCh was applied (Figure 4C and 4D). The differences in adaptation index across the three conditions were found to be significantly different by repeated measures ANOVA in somatic recordings (control 0.43 ± 0.07, CCh -0.36 ± 0.09, CCh+SKF -0.24 ± 0.10; $F(2,14) = 42.453$; $p < 0.0005$; $n = 8$; Figure 4C4) and dendritic recordings (control 0.47 ± 0.11, CCh -0.24 ± 0.07, CCh+SKF -0.23 ± 0.06; $F(2,14) = 118.541$; $p < 0.0005$; $n = 8$; Figure 4D4). However, Bonferroni-adjusted pairwise comparisons demonstrated that the significant differences lie both between control and CCh (soma $p < 0.0005$; dendrite $p < 0.0005$) and control and CCh+SKF (soma $p = 0.001$; dendrite $p < 0.0005$), not between CCh and CCh+SKF (soma $p = 0.68$; dendrite $p = 1.00$). Thus, SKF96365 did not significantly shift the adaptation index in the same manner as did FFA, suggesting that the TRP channels involved in the CCh-mediated forward shift are not of the TRPC subtype.

TRPM4 channels have likewise been implicated in downstream effects associated with G_q-coupled signaling (Launay et al., 2002; Dutta Banik et al., 2018). TRPM4 channels are activated by Ca^{2+} binding to the cytoplasmic side combined with depolarization (Nilius et al., 2003; Autzen et al., 2018), but these channels are impermeable to Ca^{2+}. Instead, TRPM4 channels facilitate a rise in $[Ca^{2+}]_i$ indirectly, by depolarizing the membrane potential (Launay et al., 2002) and therefore activating voltage-gated Ca^{2+} channels (Li et al., 2021). Cationic current through these channels and the resulting $[Ca^{2+}]_i$ elevation has been implicated in bursting, persistent firing, and oscillatory activity in some neurons (Lin et al., 2017; O'Malley et al., 2020; Li et al., 2021). In order to investigate the involvement of TRPM4 channels in the cholinergic-mediated shift in adaptation index, the TRPM4 channel antagonist CBA (50 μM) was added after recording the response to CCh (Figure 5A and 5B). Repeated measures ANOVA showed significant differences in the adaptation indices in somatic recordings (control 0.29 ± 0.05, CCh -0.37 ± 0.10,

289 CCh+CBA 0.17 ± 0.07; $F(2,16) = 66.257$; $p < 0.0005$; $n = 9$; Figure 5A4) and dendritic recordings (control
290 0.39 ± 0.07, CCh -0.41 ± 0.10, CCh+CBA 0.08 ± 0.05; $F(2,16) = 34.848$; $p < 0.0005$; $n = 9$; Figure 5B4).
291 Bonferroni-corrected pairwise comparisons indicated that for somatic recordings, the differences were
292 significant between control and CCh ($p < 0.0005$), and between CCh and CCh+CBA ($p < 0.0005$), but not
293 between control and CCh+CBA ($p = 0.16$). For dendritic recordings, Bonferroni-corrected pairwise
294 comparisons showed that the differences were significant between control and CCh ($p < 0.0005$), between
295 CCh and CCh+CBA ($p = 0.002$), and between control and CCh+CBA ($p = 0.02$). In most cells, the
296 adaptation index became negative in CCh and reverted to a positive value with the addition of CBA, and
297 in all cases the adaptation index was higher in CCh+CBA than in CCh alone.

298 In order to corroborate that the effect of CBA is due to block of TRPM4 channels, we investigated the effect
299 of a second TRPM4 channel antagonist, 9-phenanthrol, added to CCh in somatic recordings. Figure 5C
300 illustrates the shift of most of the spiking activity towards the up-ramp, moving the adaptation index in the
301 positive direction, when 9-phenanthrol (100 μM) was applied on top of CCh. The differences in adaptation
302 index between groups are significant, as demonstrated by repeated measures ANOVA (control 0.40 ±
303 0.03, CCh -0.14 ± 0.06, CCh+9Ph 0.19 ± 0.06; $F(2,14) = 57.640$; $p < 0.0005$; $n = 8$; Figure 5C4). Bonferroni-
304 corrected pairwise comparisons indicated that the differences were significant between control and CCh
305 ($p < 0.0005$), between CCh and CCh+9Ph ($p = 0.001$), and between control and CCh+9Ph ($p = 0.03$).

306 Taken together, these data with the non-selective TRP channel blocker FFA, the TRPC channel blocker
307 SKF96365, and two different TRPM4 channel antagonists suggest that the shift in adaptation index that
308 we see with CCh is largely mediated through activation of TRPM4, rather than TRPC, channels.

309

310 *Does Ca^{2+} release from internal sources activate TRPM4 channels?*

311 We next tried to determine the source of Ca^{2+} required to activate TRPM4 channels. We first focused on
312 IP_3 receptors (IP_3Rs), which are activated through mAChRs and G_q as described above, using the
313 antagonist Xestospongin C (Gafni et al., 1997) in the intracellular solution (Figure 6A). Since the
314 antagonists rapidly dialyzed into the cytosol, in this figure control data reflect the effect of the antagonists
315 before the addition of CCh. We initially used Xestospongin C at 1 μM, which was previously found to be
316 effective in inhibiting TRPM4 channel activation via mGluRs in neurons of the preBötzinger nucleus (Pace
317 et al., 2007). Since this concentration was not effective in preventing the cholinergic shift in the center of
318 mass of firing in our experiments, in six out of nine experiments we increased the concentration to 2 μM.
319 Neither concentration of intracellular Xestospongin C appeared to change the firing features in control
320 conditions. The shift induced by carbachol did not appear to depend on the concentration of Xestospongin
321 C (Figure 6A3), therefore we averaged the data in these two conditions. The adaptation index still
322 decreased significantly ($t(8) = 10.574$, $p < 0.0005$; $n = 9$, as per a paired t-test) from 0.31 ± 0.02 in control

conditions to -0.38 ± 0.07 in the presence of CCh (2 μM). This result argues strongly against the hypothesis that the effects of the activation of muscarinic receptors on the shift of the center of mass of firing are mediated by activation of IP_3Rs. Ryanodine receptors (RyRs) are also expressed on the endoplasmic reticulum in CA1 pyramidal neurons, and appear to contribute selectively to spine Ca^{2+} elevations during LTP at the CA3-CA1 synapses (Raymond and Redman, 2006). We therefore tested the hypothesis that the increase of $[Ca^{2+}]_i$ in a nanodomain leading to TRPM4 channel activation could be due to Ca^{2+}-induced Ca^{2+} release (CICR) through RyRs following Ca^{2+} influx through voltage-dependent Ca^{2+} channels. In these experiments, we included ryanodine at 40 μM, a concentration known to inhibit RyRs (Ehrlich et al., 1994; Isokawa and Alger, 2006), in the intracellular solution. Notably, one out of nine of the neurons recorded from in these conditions had a slightly negative adaptation index already under control conditions (Figure 6B3) when RyR were inhibited. Moreover, three more neurons appeared to fire irregularly, with some doublets, under control conditions (an example is shown in Figure 6C), a feature that was not observed in other experimental conditions. This change could be due to the close juxtaposition of RyRs in the endoplasmic reticulum and various K^+ channels on the membrane of CA1 neurons (Vierra et al., 2019; Tedoldi et al., 2020; Sahu and Turner, 2021). Upon addition of CCh in the bath, the adaptation index became significantly more negative in all nine neurons recorded with intracellular ryanodine, as per a paired t-test (control 0.28 ± 0.05, CCh -0.46 ± 0.07; $t(8) = 11.99$; $p < 0.0005$; $n = 9$), suggesting that RyRs also do not play a role in the cholinergic shift of the center of mass of firing.

Multicompartmental modeling of cholinergic modulation of asymmetric firing responses

We next turned to our detailed multicompartmental model, in order to help identify the underlying mechanisms that contribute to the cholinergic modulation that we observe experimentally *in vitro*. The model was implemented in a reconstructed morphology (Megías et al., 2001) with 144 compartments, each of which can be represented with an equivalent circuit with heterogeneous channel conductance densities and kinetics as described in the Methods. Previously (Upchurch et al., 2022), this model was used to capture the firing rate adaptation observed under control conditions as shown in Figure 7A1 for short triangular ramps of injected current. The model performs a material balance on Ca^{2+} ions to provide estimated free Ca^{2+} concentrations in concentric shells beneath the membrane, as shown in the top panels of Figure 7. The control simulation for a 2 second somatic ramp in Figure 7A1 captures the experimentally observed decrease in spike number and frequency on the down-ramp as compared to the up-ramp (adaptation index = 0.28), as well as a slight decrease in spike amplitude, previously shown to be due to a decrease in available Na_V channels (Upchurch et al., 2022). The plot of instantaneous frequency versus level of injected current at the right captures the clockwise pattern observed in Figure 1C1 and G1 corresponding to firing rate adaptation. Figure 7A2 shows the $[Ca^{2+}]$ in the outer shell of the soma in nM, Figure 7A3 replots this same concentration in μM (the nanodomain in this case is contiguous with the outer

shell so it is not actually a nanodomain), and Figure 7A4 shows that this concentration is insufficient to activate TRPM4 channels. In order to model the effect of CCh, we added a nanodomain for the spatially restricted Ca^{2+} concentration which we hypothesize is sensed by the Ca^{2+} binding site on TRPM4 channels; also note that, as in the experiments, the amount of injected current is lower for the simulated CCh. We showed in Figure 6 that TRPM4 channel activation is not affected by antagonists of IP_3Rs and RyRs, excluding a contribution of Ca^{2+} release from the ER. Although the source of the Ca^{2+} increase that activates TRPM4 channels is currently unknown, it likely depends in some way upon the activation of voltage-gated Ca^{2+} channels during the ramp. We therefore made the Ca^{2+} influx in the nanodomain proportional to the total instantaneous Ca^{2+} current across the membrane in the model, but only during simulated activation of the muscarinic receptor. Adding the Ca^{2+} influx from an unknown source to a nanodomain in order to simulate bath application of CCh (Figure 7B1) replicates the experimentally observed shift in adaptation index, with more spikes occurring on the down-ramp as compared to the up-ramp (adaptation index = -0.29). The plot of instantaneous frequency versus injected current captures the more extreme observed effect of CCh as illustrated in Figure 1G2; the motion is counter-clockwise corresponding to the acceleration of the firing rate. Figure 7B2 shows the Ca^{2+} concentration in the outer shell of the soma in nM, Figure 7B3 shows the Ca^{2+} concentration in μM in the hypothesized nanodomain, and Figure 7B4 shows that this concentration is sufficient to activate TRPM4 channels.

Figure 8 shows why spike rate adaptation is not observed in the simulated presence of CCh. Figure 8A repeats the voltage and current traces from the previous figure, except that the simulated CCh traces (magenta) are superimposed over the control traces (black). Our model includes a four state Markov model of the Na_V channel (see Methods). Occupancy in the open state between action potentials is the substrate for the persistent Na_V current during the interspike interval. Figure 8B shows that the occupancy in the open state of the Markov model of the Na_V channel in the soma is not greatly different between the two conditions, except for excursions produced by spiking, and Figure 8D shows the same result for the somatic Na_V current. Our previous work (Upchurch et al., 2022) attributed spike rate adaptation to reduced persistent Na_V current due to increased long-term inactivation. Figure 8C shows that although long-term inactivation of the Na_V channel (occupancy in the I2 state) starts later in simulated CCh, it eventually progresses to higher levels than in control because of the increased number of spikes. Nonetheless, no spike rate adaption was observed in simulated CCh in Figure 7B1 because the TRPM4 current is about 4-fold larger than the persistent Na_V current (compare Figures 8D and 8E). Figure 8F shows that the additional TRPM4 current more than compensates for the smaller level of injected ramp current; as a consequence, the net inward current is comparable on the up-ramp and larger in magnitude during the down-ramp for the simulated CCh case than control. This causes spiking to persist longer despite higher levels of Na_V channel inactivation.

When activated by Ca^{2+}, TRPM4 channels cause a depolarization and additional spiking that further increases Ca^{2+} influx resulting in a positive feedback loop, with the regenerative inward TRPM4 current contributing to action potential initiation. Figure 9 elaborates on the mechanisms by which Ca^{2+} and voltage differentially contribute to TRPM4 channel activation in removing or reversing spike frequency adaptation. It repeats the traces in control (black) and simulated CCh (magenta) from Figure 7 on an expanded scale and adds two conditions as described below. The insets to the right in Figure 9A show f/I curves that capture the qualitative features of the f/I curves shown in Figure 1C1, C2, G1 and G2. Qualitatively, in control (black traces), there are more spikes on the up-ramp than on the down-ramp, and the instantaneous frequency is lower on the down-ramp for similar values of injected current during the up- ramp. The contribution of the increase in Ca^{2+} concentration in the nanodomain was examined by turning off the voltage-dependence of the TRPM4 channel (light blue traces). In this case, the voltage component of TRPM4 channel activation was set to its steady state value at the resting V_m (see Methods).

Simply adding the nanodomain accomplishes the shift in center of mass (compare blue trace in Figure 9A to control trace in black) and removes the adaptation, with a very slight tendency to accelerate the firing. However, without the contribution of the voltage-dependence of TRPM4 channels, the resulting Ca^{2+} influx is lower than in the original simulation of the effects of CCh (compare the blue traces to the magenta traces in Figure 9B and C), resulting in less TRPM4 channel activation (compare the blue trace to the magenta trace in Figure 9D) and therefore fewer total spikes. To determine the contribution of the positive feedback loop by which Ca^{2+} entry recruits more Ca^{2+} entry via additional spiking and depolarization, we recorded the Ca^{2+} traces in each nanodomain (one for each segment of every section in NEURON, see Methods) of the original CCh simulation (magenta trace in Figure 9C). We then used this Ca^{2+} trace as the $[Ca^{2+}]$ in the nanodomain during simulations with the voltage dependence removed as described above. The purple trace in Figure 9A shows that the positive feedback loop added two spikes (16 in the purple trace versus 14 in the blue trace) by slightly increasing the frequency during the spike train and allowing spiking to continue longer. The f/I plot shows a little more acceleration of the firing rate. The purple trace in Figure 9B shows that $[Ca^{2+}]$ in the outermost shell is slightly different than both the blue and magenta traces, reflecting the different numbers of spikes. Note that the purple and magenta traces in Figure 9C are identical because the magenta trace for $[Ca^{2+}]$ in the nanodomain (original CCh simulation) was input to the nanodomain in the simulations shown in purple in the other panels. The additional TRPM4 channel activation (compare purple to blue trace in Figure 9D) results from the increased $[Ca^{2+}]$ in the nanodomain. Adding the full voltage-dependence to the TRPM4 channel slightly raises the overall level of TRPM4 channel activation. The voltage-dependence also allows for fast excursions in channel activation that could contribute to action potential initiation (compare magenta trace in Figure 9D to the blue and purple ones). The voltage-dependence contributes one additional spike (17 in the magenta trace versus 16 in the purple trace in Figure 9A) and accentuates spike rate acceleration due to the positive feedback loop, as shown in the f/I curves.

Evidence for tight coupling between TRPM4 channels and the calcium source that activates them

In order to test experimentally the model prediction that the highly localized Ca^{2+} elevation in a nanodomain next to the TRPM4 channels gives rise to the CCh-mediated shift in the center of mass of firing, the calcium chelator BAPTA was included in the recording pipette, and somatic recordings obtained before and during addition of CCh. In Figure 10, control data reflect the effect of BAPTA before the addition of CCh, rather than control data such as in previous figures, because the dialysis occurred quickly. As in previous sets of experiments, the amount of current injected was chosen in order to achieve a target firing frequency of 10-25 Hz. With intracellular dialysis of BAPTA, the current needed to reach these frequencies was consistently higher in these experiments (compare scale bars of injected current to those in previous figures). In addition, intracellular dialysis with BAPTA tended to shift the firing earlier in the ramp, with fewer spikes on the down-ramp, therefore making the adaptation index closer to 1. In Figure 10A, 10 mM BAPTA was included in the internal solution. As previously noted, the addition of CCh in the bath caused a depolarization that was compensated for by the injecting hyperpolarizing current. Moreover, despite the presence of BAPTA, the adaptation index became significantly smaller in the presence of CCh, as per a paired t-test (control 0.82 ± 0.05, CCh -0.12 ± 0.11; $t(9) = 8.594$; $p < 0.0005$; $n = 10$; Figure 10A3); therefore, 10 mM BAPTA did not prevent the cholinergic-mediated shift. It has been shown that a higher concentration of BAPTA may be required to prevent TRPM4 channel activation in neurons of the preBötzinger nucleus (Pace et al., 2007; Picardo et al., 2019), therefore, in Figure 10B, BAPTA in the internal solution was increased to 30 mM. With a free $[Ca^{2+}]_i$ of 100 nM (see Methods), CCh never produced negative adaptation indices that were seen in previous figures, although the V_m did depolarize and was restored by the injection of tonic hyperpolarizing current. CCh still had a significant effect on the adaptation index, as per a paired t-test (control 0.62 ± 0.05, CCh 0.37 ± 0.06; $t(7) = 5.069$; $p = 0.001$; $n = 8$; Figure 10B3). However, when the free $[Ca^{2+}]_i$ was adjusted to 10 nM in the presence of intracellular 30 mM BAPTA (Figure 10C), the adaptation index did not change significantly when CCh was applied in the bath (control 0.73 ± 0.03, CCh 0.76 ± 0.03; $t(11) = 0.776$; $p = 0.45$; $n = 12$; Figure 10C3). In addition, the depolarization normally observed in the presence of CCh did not occur in these conditions, and the amount of injected current was comparable to that injected in control. These data demonstrate that a concentration of BAPTA higher than the typical value (10 mM) used to disrupt Ca^{2+}-dependent mechanisms (Harney et al., 2006) is required to prevent TRPM4 channel activation, and that free $[Ca^{2+}]_I$ of <100 nM is necessary to disrupt TRPM4 channel activation. Together, these data suggest a close physical relationship between the source of Ca^{2+} and TRPM4 channels.

Discussion

Summary of major results

463 Whereas place cell firing can only be observed *in vivo*, our bidirectional approach of modeling place cell
464 firing *in vitro* and *in silico* can be precisely targeted to uncover molecular mechanisms responsible for
465 modulation of firing patterns that lead to place cell firing *in vivo*. Manipulations that are difficult or impossible
466 even in the *in vitro* preparation can be carried out *in silico* using our detailed multicompartmental model,
467 with the added benefit that the model is transparent. All underlying state variables (ion concentrations,
468 channel open fractions) are accessible so that mechanisms can be positively identified, facilitating design
469 of experiments to test the putative mechanisms.

470 In this study we show that: 1) muscarinic receptor activation shifts the center of mass of firing from earlier
471 to later during a depolarizing ramp, through 2) activation of I_{CAN} mediated by TRP channels, most likely of
472 the TRPM4 subtype; 3) the shift is not affected by the inhibition of either IP_3Rs or RyRs, arguing against a
473 role of Ca^{2+} released from the endoplasmic reticulum in this process; 4) multicompartmental modeling
474 suggests a close physical relationship between the source of Ca^{2+} increase and the TRPM4 channels; 5)
475 the model prediction is supported by recordings showing that a very high concentration of BAPTA (30 mM),
476 combined with buffering $[Ca^{2+}]_i$ at 10 nM are required to prevent the cholinergic-mediated rightward shift.

477 More broadly, our results suggest that some rapid changes to place cell firing could be triggered via
478 neuromodulation of intrinsic excitability, in addition to and distinct from longer lasting experience-
479 dependent changes that are brought about by synaptic and structural plasticity. Specifically, we speculate
480 that increasing levels of ACh could lead to forward shifts in place cell firing, whereas decreasing levels of
481 ACh could contribute to backwards shifts.

482

483 *Mystery current identified*

484 Muscarinic activation of a Ca^{2+}-dependent nonselective cation current in rat CA1 pyramidal neurons has
485 been known for nearly three decades (Colino and Halliwell, 1993; Fraser and MacVicar, 1996; Dasari et
486 al., 2017). A previous study (Yamada-Hanff and Bean, 2013) found that in mouse CA1 neurons as well,
487 muscarinic stimulation not only inhibits background potassium currents but also activates a nonselective
488 cation current. They found that the latter effect was dominant and in fact converted CA1 pyramidal neurons
489 into pacemakers with the application of 5-25 μM acetylcholine, 5-25 μM carbachol, or 5-10 μM
490 oxotremorine-M. They suggested TRPC channels might mediate this current but were unable to positively
491 identify the source of the nonselective cation current. Based on our results, this unidentified channel could
492 be the TRPM4 channel. We show that TRPM4 channels primarily mediate a nonspecific Ca^{2+}-activated
493 cation current evoked by cholinergic modulation in CA1 pyramidal neurons. Our model shows that the
494 activation of TRPM4 channels contribute an additional inward current that activates and deactivates slowly
495 upon depolarization. In the case of synaptically-driven depolarizations (Figure 2), this inward current, with
496 its slow kinetics (see Figures 8 and 9) is likely to cause an increased decay time of the EPSPs (see Figure

497 2). This aspect has likely implications for synaptic integration by these neurons, as shown by the
498 observation of an impairment of LTP in TRPM4 knockout mice (Menigoz et al., 2016).

499 One of our most surprising findings was that TRPC channels did not seem to play a role in cholinergic
500 modulation of the firing pattern along a triangular ramp. TRPC channels have been implicated in cholinergic
501 signaling via direct activation by DAG, one of the two bioactive molecules generated by PLC hydrolysis of
502 PIP_2 (the other being IP_3). Cholinergic-associated persistent firing, whereby neurons continue to fire after
503 a depolarizing stimulus has ceased, has been attributed to activation of TRPC channels (Zhang et al.,
504 2011; Arboit et al., 2020). However, the presence of cholinergic-induced persistent firing in TRPC knockout
505 mice has called this into question (Egorov et al., 2019). In a recent study, TRPM4 channels were found to
506 be involved in persistent firing generated upon Ca^{2+} influx via T-type channels in thalamic neurons
507 (O'Malley et al., 2020). Delayed bursting in a subtype of cerebellar granular cells was also shown to be
508 mediated by TRPM4 channels (Masoli et al., 2020). Our study therefore provides further evidence
509 regarding the role of these channels in the control of neuronal firing, possibly including persistent firing.

510

511 *Nanodomain resulting from colocalization of cholinergic-induced increases in $[Ca^{2+}]_i$ and TRPM4 channels*

512 In HEK cells transfected with cDNA encoding TRPM4 channels, and in cardiac myocytes, activation of
513 TRPM4 channels is secondary to IP_3 receptor activation (Launay et al., 2002; Gonzales et al., 2010;
514 Gonzales and Earley, 2012), suggesting that TRPM4 channels in myocytes are activated by Ca^{2+} release
515 from intracellular stores. Furthermore, in situ proximity ligation assay was used to demonstrate co-
516 localization of TRPM4 channels and IP_3Rs in human detrusor smooth muscle cells (Provence et al., 2017).
517 In addition, in neurons of the preBötzinger nucleus TRPM4 channels are recruited by metabotropic
518 glutamate receptors to generate robust inspiratory drive potentials through IP_3R activation (Pace et al.,
519 2007). Surprisingly, we found that Ca^{2+} release from the ER was not involved in the cholinergic shift of the
520 center of mass of firing, since neither the IP_3R antagonist Xestospongin C (1-2 μM) nor the RyR antagonist
521 ryanodine (40 μM) prevented the effects of carbachol. Therefore, although the mechanisms that
522 produce the micromolar $[Ca^{2+}]$ increases needed for TRPM4 channel activation are unknown, our results
523 point to these channels acting as coincidence detector, requiring both muscarinic receptor activation and
524 depolarization-induced Ca^{2+} influx during the ramp to be activated

525 Our modeling results imply that, upon activation of muscarinic receptors, TRPM4 channels have privileged
526 access to a nanodomain in order to achieve the micromolar concentrations of Ca^{2+} necessary for their
527 activation (Nilius et al., 2004), since microdomains (like the multicompartmental model's outer shell) only
528 achieve submicromolar concentrations (Fakler and Adelman, 2008). The affinity of TRPM4 channels for
529 Ca^{2+} is heavily dependent on the availability of PIP_2 (Nilius et al., 2006) and binding of ATP and calmodulin
530 or PKC-dependent phosphorylation (Nilius et al., 2005), which all function to increase the sensitivity of

531 TRPM4 channels for Ca^{2+}. If under our conditions, the dependence of TRPM4 channels on [Ca^{2+}] has a
532 much lower EC_{50} and/or is much steeper than in the model we implemented (Nilius et al., 2004), perhaps
533 the nanomolar [Ca^{2+}] in the outer shell could be sufficient to activate TRPM4 channels. However, the
534 experimental result that 30 mM BAPTA was required to block the TRPM4 channels' access to Ca^{2+} argues
535 for a spatially restricted nanodomain. In a previous study, we found that intracellular BAPTA at a
536 concentration 5 mM can mimic SK block (Combe et al., 2018), presumably by interfering with the calcium
537 activation of those channels. The requirement of using 30 mM BAPTA while buffering free $[Ca^{2+}]_i$ to 10
538 nM in order to prevent TRPM4 channel activation suggests that TRPM4 channels are activated by a more
539 spatially restricted Ca^{2+} domain than SK channels.

540

541 *Convergence of pharmacological blockers*

542 One caveat for our experimental results is that TRP channel blockers, like most drugs, have been reported
543 to have some non-specific effects. In cardiac cells, both CBA and 9-phenanthrol have been shown to
544 decrease the Ito1 potassium current, attributed to Kv4.3 (Veress et al., 2018; Dienes et al., 2021) and a
545 late sodium current (Hou et al., 2018; Dienes et al., 2021). Kv4.3 is likely more important in interneurons
546 than in pyramidal cells in the CA1 area (Martina et al., 1998), and neither of the two currents are affected
547 by FFA at the concentration we used here (Guinamard et al., 2013). The other reported non-specific effects
548 do not overlap between the three blockers, flufenamic acid, CBA and 9-phenanthrol (Simard et al., 2012;
549 Guinamard et al., 2013; Veress et al., 2018; Dienes et al., 2021). The convergent effects of these three
550 distinct drugs implicate TRPM4 channels as the most probable effector of the CCh-mediated modulation
551 of the center of mass of firing. A similar pharmacological approach was used to implicate TRPM4 channel
552 activation in subthreshold oscillations underlying pacemaker firing of chemosensory neurons in the
553 retrotrapezoid nucleus (Li et al., 2021).

554

555 *Diverse cholinergic effects on CA1 pyramidal neurons*

556 In CA1 pyramidal neurons, ACh binding to muscarinic receptors results in neuromodulation of neuronal
557 excitability and presynaptic release probability. In our study, focused mainly on intrinsic properties, the
558 predominant effect of ACh and CCh was to activate TRPM4 channels; however, the effect of ACh on CA1
559 pyramidal cells *in vivo* is multipronged. Muscarinic receptors are known to suppress several K^+ currents in
560 CA1 pyramidal neurons (Halliwell and Adams, 1982; Hoffman and Johnston, 1998; Buchanan et al., 2010;
561 Giessel and Sabatini, 2010). The effects of ACh on SK, M-type currents and I_{CAN} are mediated by M_1 (G_q-
562 coupled) receptors (Dasari and Gulledge, 2011). Synaptic depression of Schaffer collateral inputs to CA1
563 is mediated by M_4 (G_i-coupled) receptors (Dasari and Gulledge, 2011) located on presynaptic
564 glutamatergic terminals, and synaptic depression of temporoammonic pathway glutamatergic inputs to

565 CA1 is mediated by M_3 (G_q-coupled) receptors (Palacios-Filardo et al., 2021). When we used a synaptically-
566 driven depolarization (Figure 2), decreased release from Schaffer collateral was indicated by the smaller
567 amplitude EPSPs in the presence of CCh. In these experiments, as in the current injection protocols, the
568 center of mass of firing occurred earlier in the ramp in control and shifted to later in the ramp in the presence
569 of CCh, suggesting that a combination of pre- and postsynaptic effects of cholinergic agonists can
570 contribute to the shift. Moreover, the cholinergic down-regulation of these afferents justifies the use of
571 smaller depolarizing current injection ramps in our recordings in the presence of carbachol, because less
572 current injection is required to produce the same output frequencies due to enhanced intrinsic excitability
573 in carbachol.

574 In a model of place field formation (Savelli and Knierim, 2010), if a neuron randomly fires within a place
575 field (Bittner et al., 2015), its inputs from the currently active grid cells are strengthened and the input from
576 those grid cells onto silent cells are weakened. Previously, ACh was thought to act in a manner consistent
577 with volume transmission (Dannenberg et al., 2017). Recently, this view has been challenged by the finding
578 that all hippocampal cholinergic terminals form synapses (Takács et al., 2018), and vesicles dock only at
579 synapses. Since cholinergic neuromodulation of TRPM4 channels greatly increases excitability in CA1
580 pyramidal cells, selective synaptic ACh inputs may underlie the formation of place fields in a novel
581 environment. Moreover, (Takács et al., 2018) found that the ACh terminals co-released GABA in separate
582 vesicles, and that ACh acting on M_2 (G_i-coupled) autoreceptors on cholinergic terminals inhibited the
583 release of both ACh and GABA. Future work is required to disentangle the distinct effects of ACh acting at
584 the various muscarinic receptors (M_1-M_5).

585

586 *Acetylcholine, Novelty and Place Field Shifts*

587 Acetylcholine acting at muscarinic receptors has been hypothesized to be a global novelty signal in the
588 dentate gyrus (Gómez-Ocádiz et al., 2022), dorsal hippocampus (Huff et al., 2022), and the
589 parahippocampal gyrus (Frank and Kafkas, 2021). A novel unconditioned stimulus caused a large increase
590 in ACh extracellular levels in the hippocampus, but little locomotion (Acquas et al., 1996). On the other
591 hand, hippocampal ACh release in an animal placed in a novel environment has two components, one
592 related to novelty, that disappears in a familiar environment (Thiel et al., 1998), and one related to motor
593 activity, associated with increased exploration (Giovannini et al., 2001). Indeed, a recent fiber photometric
594 study showed that part of the population activity in medial septal cholinergic neurons is correlated with the
595 logarithm of running speed (Kopsick et al., 2022). We are primarily interested in the component of the ACh
596 signal related to novelty because of previous studies demonstrating modulation of place cell firing that was
597 more pronounced during the first day in a novel environment (Roth et al., 2012).

598

599 *In vivo* recordings in rats demonstrated that place fields expand and the center of mass shifts backward
600 with respect to the direction of travel on continuous tracks over several laps during each recording session
601 (Mehta et al., 2000). This phenomenon was predicted by modeling studies that implemented Hebbian
602 plasticity in the form of NMDA-mediated LTP (Abbott and Blum, 1996; Blum and Abbott, 1996), whereby
603 spatially tuned input gradually strengthens over repeated traversals of a place field, causing a CA1 place
604 cell to fire earlier in the place field. NMDA blockers were subsequently shown to occlude the backwards
605 shift of the place field (Ekstrom et al., 2001) and an NMDA agonist partially restored it in aged rats (Burke
606 et al., 2008). Calcium imaging in mice running on a treadmill in a virtual environment showed an abrupt
607 backward shift in place cell firing (relative to where the first episode of place field firing occurred) during
608 the first exposure to a novel environment (Priestley et al., 2022), as well as much smaller backward shifts
609 in place fields in novel environments that leveled off as the animals became more familiar with the
610 environment during subsequent exposures (Dong et al., 2021). These backwards shifts, which were much
611 larger than those observed previously and attributed to Hebbian plasticity, were ascribed to behavioral
612 time scale plasticity, which is also dependent on NMDA receptor activation, and strengthens glutamatergic
613 inputs active during an asymmetric seconds-long window skewed towards synapses activated before a
614 burst triggered by a dendritic plateau (Bittner et al., 2017).

615 Despite the ability of elegant theories of synaptic plasticity to account for backward shifts in the center of
616 mass of the place field, forward shifts have also been observed. Forward shifting of the center of mass of
617 place field firing occurred, shifting toward prospective goal locations in the continuous T-maze alternation
618 task as a reward was approached (Lee et al., 2006). Thus, task-specific demands may allow for the
619 modulation of firing fields by neuromodulators such as ACh and dopamine. In a study that did not involve
620 reward, but only exploration of a novel virtual linear maze (Dong et al., 2021), the center of mass of CA1
621 place fields in laps 2-4 were forward shifted compared to the first lap, for cells that already had a place
622 field on the first lap (a lap required approximately 25 seconds). Laps 5 and beyond were backward shifted
623 compared to the immediately preceding lap, so averaging over all runs, the place field was shifted
624 backwards. Perhaps the neuromodulatory environment, including cholinergic tone, was different during the
625 first four laps. The data in that study indicated that backward shifting in CA1 in a novel environment is due
626 to a combination of place field expansion, skewness and translation of the point at which peak firing occurs.
627 They suggested that since skewness and width dynamics are inconsistent across studies, multiple
628 mechanisms may be involved in place field shifting.

629

630 *Ideas and Speculations: Implications of our results for place fields in intact rodents*

631 Our results suggest that increasing levels of ACh could lead to forward shifts in place field center of mass
632 whereas decreasing levels of ACh could contribute to backwards shifts. Since cholinergic activity in CA1
633 is elevated when animals encounter novel environments, our results with CCh could correspond to an

634 initial encounter with a novel environment, where firing of an existing place cell is shifted “forward” or later
635 during the depolarizing ramp that simulates spatially-tuned input. Our control conditions, then, would be
636 analogous to lower cholinergic tone, occurring as an animal becomes familiar with an environment, and
637 the associated “backward” shift earlier in the depolarizing ramp. The rapid modulation of ion channels by
638 removal of cholinergic tone could therefore provide a possible mechanism for the rapid shifting of place
639 cell firing in a novel versus familiar environment, perhaps complementary to Hebbian plasticity that
640 develops over time.

641 If our hypothesis is correct, optogenetic silencing of medial septum cholinergic afferents to CA1 during
642 runs through a place field in a novel environment should partially occlude backwards shifts in place field
643 center on subsequent runs that are due to diminished ACh in a familiar environment. Optogenetic
644 stimulation of the same afferents during runs in a familiar environment should induce forward shifts in place
645 field centers. Behaviorally, it could be informative to design experiments to test the effects of these
646 manipulations on the animal’s subjective sense of position, for example, demonstrated by overshoot or
647 undershoot locations where the animal has been trained to pause.

648 There is a growing realization that there may be multiple mechanisms for place field shifting in addition to
649 the well-known mechanisms for backwards shifts dependent on Hebbian plasticity (Blum and Abbott, 1996;
650 Ekstrom et al., 2001; Burke et al., 2008; Roth et al., 2012; Mehta et al., 2000) or, more recently, behavioral
651 timescale synaptic plasticity (Bittner et al., 2017; Priestley et al., 2022). We propose that neuromodulation
652 of intrinsic properties by ACh, and potentially other neuromodulators like dopamine, provide an additional
653 level of modulatory control in parallel with synaptic plasticity mechanisms, contributing to rapid place field
654 shifts.

655

656 **Materials and Methods**

Key Resources Table				
Reagent type (species) or resource	**Designation**	**Source or reference**	**Identifiers**	**Additional information**
Strain, strain background	Male Sprague Dawley rats	Envigo (Inovit)	Hsd:Sprague Dawley® SD®	7-12 weeks old when sacrificed for experiments
chemical compound, drug	NBQX	Alomone Labs	cat# N-186	AMPA receptor antagonist

chemical compound, drug	DL-APV	HelloBio	cat# HB0252	NMDA receptor antagonist
chemical compound, drug	Gabazine	Alomone Labs	cat# G-216	$GABA_A$ receptor antagonist
chemical compound, drug	CGP55845	Abcam	cat# ab120337	$GABA_B$ receptor antagonist
chemical compound, drug	Carbachol	Tocris	cat# 2810	Acetylcholine receptor agonist
chemical compound, drug	Acetylcholine,	Sigma-Aldrich	cat# A6625	Ligand for acetylcholine receptors
chemical compound, drug	flufenamic acid	Sigma-Aldrich	cat# F9005	TRP channel antagonist
chemical compound, drug	SKF96365	Alomone Labs	cat# S-175	TRPC channel antagonist
chemical compound, drug	CBA	Tocris	cat# 6724	TRPM4 channel antagonist
chemical compound, drug	9-phenanthrol	Tocris	cat# 4999	TRPM4 channel antagonist
chemical compound, drug	Xestospongin C	Abcam	cat# ab120914	IP_3R antagonist
chemical compound, drug	low molecular weight heparin	Sigma-Aldrich	cat# H3149	IP_3R antagonist
chemical compound, drug	D-myo-IP_3	Cayman Chemical	cat# 60960	IP_3R agonist
chemical compound, drug	Adenophostin A	MilliporeSigma	cat# 115500	IP_3R agonist
chemical compound, drug	Ryanodine	HelloBio	cat# HB1320	RyR antagonist at [μM]

chemical compound, drug	Ruthenium red	Tocris	cat# 1439	RyR antagonist
chemical compound, drug	Dantrolene	Tocris	cat# 0507	RyR antagonist
chemical compound, drug	caffeine	Tocris	cat# 2793	RyR agonist
chemical compound, drug	Thapsigargin	Alomone Labs	cat# T-650	SERCA inhibitor
chemical compound, drug	BAPTA tetra-potassium salt (K4-BAPTA)	Sigma-Aldrich	cat# A9801	fast Ca^{2+} chelator
Software, algorithm	MAXCHELATOR, WEBMAXC EXTENDED	https://somapp.ucdmc.ucdavis.edu/pharmacology/bers/maxchelator/webmaxc/webmaxcE.htm		Online free metal calculator
Software, algorithm	SPSS	IBM	RRID:SCR_002865	Statistics software
Software, algorithm	NEURON	Hines and Carnevale, 1997; Carnevale and Hines, 2006	doi:10.1162/neco.1997.9.6.1179; doi.org/10.1017/CBO9780511541612	Computational modelling and simulation software
other	Laerd Statistics	https://statistics.laerd.com/		Online tutorial and software guide

Experimental methods

Slice preparation. All the procedures described below were conducted according to protocols developed by following guidelines on the responsible use of laboratory animals in research from the National Institutes of Health and approved by the Louisiana State University Health Sciences Center-New Orleans Institutional Animal Care and Use Committee (IACUC, internal protocol numbers 3583 and 3851). Animals

664 were housed in pairs, whenever possible; in the event of single housing, Bed-r'nest pucks (Andersons Lab
665 Bedding) were provided for enrichment purposes.

666 For these experiments, 400 μm-thick slices were prepared from 7 to 11-week-old male Sprague Dawley
667 rats as previously described (Combe et al., 2018). Briefly, rats were deeply anesthetized via intraperitoneal
668 injection of ketamine and xylazine (90 and 10 mg/kg, respectively), until the disappearance of the toe-pinch
669 and palpebral reflexes. After trans-cardiac perfusion with ice-cold solution, decapitation, and rapid removal
670 of the brains, transverse hippocampal slices were cut using a vibratome. Slices were then transferred to a
671 chamber filled with an oxygenated artificial cerebro-spinal fluid (ACSF) containing, in mM: NaCl 125,
672 $NaHCO_3$ 25, KCl 2.5, NaH_2PO_4 1.25, $MgCl_2$ 1, $CaCl_2$ 2, dextrose 25, ascorbate 1, sodium pyruvate 3.

673 *Patch clamp electrophysiology.* After recovery, individual slices were transferred to a submerged recording
674 chamber, and superfused with ACSF at about 2 ml/min; the solution was warmed through an inline heater
675 and measured to keep it at a temperature of 34-36°C in the chamber.

676 CA1 pyramidal cells were identified via differential interference contrast-infrared video microscopy. Whole-
677 cell current clamp recordings were made using Dagan BVC 700A amplifiers in the active "bridge" mode.
678 Recording pipettes were filled with an internal solution that contained, in mM: potassium
679 methanesulphonate 125, KCl 20, HEPES 10, EGTA 0.5, NaCl 4, Mg_2ATP 4, $Tris_2GTP$ 0.3,
680 phosphocreatine 14. The electrode resistance was 1-3 MΩ for somatic recordings and 3-5 MΩ for dendritic
681 recordings. Series resistance was monitored throughout the recordings and was usually less than 20 MΩ;
682 recordings were discarded when series resistance reached 25 MΩ or 30 MΩ, for somatic and dendritic
683 recordings, respectively. Cells with resting membrane potentials depolarized beyond -60 mV at break-in
684 were discarded.
685 To investigate the contribution of intracellular Ca^{2+} signaling to TRPM4 channel activation and the
686 cholinergic shift in the center of mass of firing, in some sets of experiments, the internal patch clamp
687 solution was modified as follows. In some experiments, EGTA was replaced by higher concentrations (10
688 or 30 mM) of the faster Ca^{2+} chelator BAPTA tetra-potassium salt. When 30 mM BAPTA was included,
689 0.69 mM or 5.7 mM Ca^{2+} was added to the internal solution to give 10 or 100 nM free [Ca^{2+}], respectively,
690 at 33°C, pH 7.3 and an overall ionic concentration of 300 mM, according to the online program
691 MAXCHELATOR, WEBMAXC EXTENDED version (https://somapp.ucdmc.ucdavis.edu/pharmacology/
692 bers/maxchelator/webmaxc/webmaxcE.htm). In other experiments, Xestospongin C (1-2 μM) or ryanodine
693 (40 μM) were added to the internal patch clamp solution to block IP_3Rs and RyRs, respectively.
694 Xestospongin C and ryanodine were dissolved in DMSO; in this case the [DMSO] in the final solution was
695 ≤ 0.2% due to the limited solubility of these compounds. As in (Pace et al., 2007), Xestospongin C was
696 added to the standard intracellular solution immediately prior to use and discarded after 2 hours. In all
697 these cases, intracellular dialysis appeared to take effect quickly, so the control data refer to the effect of

698 the modified internal solution. Nonetheless, dialysis was allowed for at least 20 minutes in these
699 experiments to make sure that the drug could diffuse into distal compartments.
700 NBQX (10 μM), DL-APV (50 μM), Gabazine (12.5 μM) and CGP55845 (1 μM) were applied in the external
701 solution in all experiments, except those in which the Schaffer Collateral fibers were electrically stimulated
702 (Figure 2), to block glutamatergic and GABAergic neurotransmission, respectively, in order to isolate the
703 contribution of the intrinsic ion channels to the ramp responses. Carbachol (2 μM), acetylcholine (2, 10, or
704 15 μM), flufenamic acid (100 μM), SKF96365 (50 μM), CBA (50 μM), and 9-phenanthrol (100 μM) were
705 added to the external solution as needed, from stock solutions made with water, DMSO, or ethanol; the
706 concentration of ethanol or DMSO in the final solution was ≤ 0.1%. Carbachol, 9-phenanthrol, and CBA
707 were purchased from Tocris, CGP55845 and Xestospongin C from Abcam (Cambridge, MA), DL-APV and
708 ryanodine from HelloBio (Princeton, NJ), NBQX, Gabazine, and SKF96365 from Alomone Labs
709 (Jerusalem, Israel), and acetylcholine, flufenamic acid, and K4-BAPTA from Sigma (St. Louis, MO).

710 In order to approximate the depolarizing input that place cells receive as an animal traverses the place
711 field, ramp-shaped depolarizing current injections were applied via the recording electrode to CA1
712 pyramidal neurons at either the soma or the apical dendrite (150-250 μm from soma). Two second ramps
713 (1 s up, 1 s down) and ten second ramps (5 s up, 5 s down) were applied to simulate different running
714 speeds. Current amplitude was adjusted to evoke peak frequencies between 10 and 25 Hz, comparable
715 to place cell firing as recorded *in vivo* (Hargreaves et al., 2007; Resnik et al., 2012; Bittner et al., 2015).

716 Electrical stimulation was achieved by delivering constant current pulses through a tungsten bipolar
717 electrode placed in the stratum radiatum of area CA1 to stimulate the Schaffer collateral fibers from CA3
718 pyramidal neurons. The instantaneous input frequency of stimulation was adjusted according to a linear,
719 symmetric ramp (see also (Hsu et al., 2018). The total duration of the ramp was ~2 s and the peak
720 frequency at the center of the ramp was 25 Hz, our target for the maximum peak frequency in the ramp
721 current injections (see above). The intensity of stimulation was adjusted such that neurons would fire in
722 response to 50-70% of the total inputs and kept constant in control conditions and in the presence of
723 carbachol. For each neuron and condition, we averaged the trials where the neurons did not fire in
724 response to the first pulse in the synaptic ramp and the amplitude of the EPSPs was measured to estimate
725 the degree of cholinergic modulation of presynaptic release. Antagonists of synaptic transmitter receptors
726 were omitted in these experiments.

727

728 *Experimental design and statistical analyses*

729 Experimental data were recorded and analyzed with Igor Pro software (WaveMetrics). Left or rightward
730 shifts in firing along the current ramp were quantified as an adaptation index, as previously described
731 (Upchurch et al., 2022):

732 $$\frac{\#APs\ on\ up\text{-}ramp - \#APs\ on\ down\text{-}ramp}{\#APs\ on\ up\text{-}ramp + \#APs\ on\ down\text{-}ramp}$$

733 Positive values indicate firing predominantly on the up-ramp, while negative values indicate firing mostly
734 on the down-ramp. For synaptically driven membrane potential ramps, the adaptation index was calculated
735 in a similar manner, where the up-ramp consisted of the first 15 (out of 30) stimuli. An adaptation index of
736 zero indicates symmetry in the number of action potentials on the up-ramp and the down-ramp. Plots of
737 instantaneous frequency versus time (f/t) or current (f/I) use the time or current value at the midpoint of the
738 interspike interval (ISI), respectively. Current amplitude is relative to tonic baseline current. Raster plots in
739 Figures 1 and 2 show the timing of action potential firing for several trials in control conditions and in the
740 presence of carbachol, where time = 0 indicates the beginning of the ramp. The tick marks represent the
741 timing of each action potential (when the V_m crossed -40 mV).

742 An n = 6-12 is required for a typical patch clamp electrophysiology experiment that has a difference in
743 means of 1.3-2X and a standard deviation of 0.2-0.3 for p = 0.05 and a power of 0.9 (Cohen, 1977). Each
744 experimental group in this study is made up of n ≥ 8 recording sessions; the number of cells recorded for
745 each experiment is indicated in the Results section. Recordings were from one cell per slice; typically, a
746 maximum of three recordings were obtained for each animal. Biological replicates (recording from different
747 cells) were n ≥ 8 for each experiment and (recordings from different animals) n ≥ 6 for each experiment.

748 Statistical analyses were performed in SPSS (IBM, RRID:SCR_002865), following the tutorials and
749 software guide from Laerd Statistics (2015, https://statistics.laerd.com/). Comparisons were made in the
750 same cell before and during pharmacological treatment; the summary plots for these data include individual
751 points and means ± standard error of the mean. Parametric analyses (paired samples t-test and repeated-
752 measures ANOVA) were used to compare treatments in the same neurons, since data were normally
753 distributed as determined by the Shapiro-Wilk test for normality. Significant differences demonstrated by
754 repeated measures ANOVA were followed up by post-hoc analysis using Bonferroni-corrected pair-wise
755 comparisons. Differences were considered to be statistically significant when $p < 0.05$. Outliers, as
756 assessed by boxplots, were not removed from analysis. To check the effect of the outliers, analyses were
757 also performed after removing outliers, and with non-parametric tests keeping the outliers. The significance
758 did not change, and for consistency, the results of parametric tests are reported with all data included.

759 *Data Availability*

760 Data generated and analyzed during the study are included in the manuscript and supporting files. Source
761 data are provided for all experimental figures.

762 *Computational Modeling*

A multicompartmental CA1 pyramidal neuron model from our laboratory was used as a starting point (Upchurch et al., 2022). This model was based on the model in the study by (Poirazi et al., 2003a), with subsequent changes made in studies by (Shah et al., 2008), (Bianchi et al., 2012), and (Combe et al., 2018). The model (Figure 11A) was created from a reconstructed morphology (Megías et al., 2001) with 144 compartments and implemented in the NEURON simulation software package (Hines and Carnevale, 1997; Carnevale and Hines, 2006). The following currents (Figure 11B) were modeled using Ohmic drive and conductances in parallel with a membrane capacitance (C_M): a Na^+ current (I_{Na}), L-type (I_{CaL}), R-type (I_{CaR}), and T-type (I_{CaT}) Ca^{2+} currents, two delayed rectifiers (I_{Kv1} and I_{Kv2}), an A-type K^+ current (I_A), an inward rectifying potassium current (I_{KIR}), a nonspecific Ca^{2+}-activated current (I_{CAN}), a hyperpolarization-activated mixed cationic h-current (I_h), and a leak current (I_L). All currents were as in the previous model except (I_{CAN}), which was added to the model. In the soma and apical dendrites, we kept the Markov model (Figure 11C) of the Na_V channel that we modified from (Balbi et al., 2017). This Markov model was tuned to replicate the distance-dependent long-term inactivation of $Na_V1.6$ found in the literature (Mickus et al., 1999) that causes spike frequency adaptation and the difference in half activation between the soma and dendrites supported by (Gasparini and Magee, 2002). The sevenfold gradient in the h-conductance supported by (Magee, 1998), sixfold gradient in A-type potassium channels supported by (Hoffman et al., 1997) and lower sodium conductance in the dendrites versus the soma (75% of somatic value) supported by (Gasparini and Migliore, 2015) were also retained. A spine factor, to account for the additional membrane area due a higher density of spines (Megías et al., 2001) was varied as described in (Upchurch et al., 2022), and a sigmoidal decrease in membrane and axial resistance was implemented to account for the decrease in input resistance along the apical dendrites (Magee, 1998; Poirazi et al., 2003b).

The calcium handling for the model (see top panels in Figure 7A1 and B1) was modified from (Ashhad and Narayanan, 2013). The model performs a Ca^{2+} material balance on four shells in each compartment, and incorporates radial and longitudinal diffusion ($D_{Ca}\nabla^2[Ca^{2+}]$), stationary and mobile Ca^{2+} buffers (R_{Buf}), calcium leak through endoplasmic reticulum leak channels (J_{leak}), Ca^{2+} uptake from a sarcoplasmic/endoplasmic reticulum Ca^{2+} ATPase pump (J_{SERCA}), IP_3-mediated Ca^{2+} release (J_{IP3R}), a plasma membrane extrusion pump (J_{Pump}) and Ca^{2+} from voltage gated channels on the membrane (J_{VGCC}). The latter two terms appear only in the outer shell. Details on the implementation of diffusion, the buffers, calcium leak and the pumps are described in (Ashhad and Narayanan, 2013). The differential equation for cytosolic calcium is described below.

$$\frac{\partial[Ca^{2+}]}{\partial t} = D_{Ca}\nabla^2[Ca^{2+}] + AJ_{IP3R} + B(J_{leak} - J_{SERCA}) + R_{Buf} + J_{VGCC} - J_{Pump}$$

We used an equation for Ca^{2+} dynamics in the nanodomain that is agnostic as to the source of the Ca^{2+} contributing to the nanodomain:

$$\frac{d[Ca^{2+}]_{ND}}{dt} = X * I_{Ca} + \frac{[Ca^{2+}]_{outer\ shell} - [Ca^{2+}]_{ND}}{400ms}$$

where X is a scale factor representing the effect of a small volume for Ca^{2+} accumulation in the restricted nanodomain. The model is agnostic regarding the source of the Ca^{2+} entry into the nanodomain, which was arbitrarily set to be proportional to the total Ca^{2+} current I_{Ca}. In the absence of simulated application of CCh, $X = 0$ so that the TRPM4 channel senses the bulk Ca^{2+} concentration in the outer shell. To simulate application of CCh, in contrast with our previous modeling efforts, based on a central role for IP_3R (see Figure 11 – Figure supplement 1), [IP3] and therefore J_{IP3R} was not increased from baseline levels; instead, influx to the nanodomain from an unknown source was simulated by setting $X = 500$. The relatively long time constant reflected the spatially restricted nature of the nanodomain, with some postulated impediment to diffusion between the nanodomain and the bulk cytosol. In one simulation (purple traces in Figure 9), the $[Ca^{2+}]_{ND}$ for every segment in every section was recorded was recorded in the original CCh simulation (magenta traces) and played back using NEURON's vector play method in the model lacking the voltage-dependence of the TRPM4 channels in order to eliminate differences in $[Ca^{2+}]_{ND}$ between models and focus solely on the contribution of the voltage-dependence unrelated to additional Ca^{2+} influx.

The TRPM4 model was modified from (Nilius et al., 2004) and assumes that the required binding of Ca^{2+} to the channel precedes voltage-dependent channel activation. The model has three different states, an unbound state, a Ca^{2+} bound closed state, and an open state.

$$TRPM4 \Leftrightarrow TRPM4\ bound\ to\ Ca^{2+} \underset{\alpha(V),\beta(V)}{\Longleftrightarrow} Open\ TRPM4\ channel$$

Ca^{2+} binding is assumed to be much faster than the voltage dependent gating and is assumed to instantaneously reach the steady state binding determined by the dissociation constant K_d (87 μM). The fraction of open channels m relaxes to the steady state activation m_∞ with a time constant, τ, with first order kinetics:

$$\alpha' = \frac{\alpha}{1+\frac{Kd}{[Ca^{2+}]_{ND}}}, m_\infty = \frac{\alpha\prime}{\alpha'+\beta} \qquad \tau = \frac{1}{\alpha'+\beta}$$

where α is the forward rate of Ca^{2+} bound TRPM4 channel opening, $\alpha(V) = 0.0057 \exp(0.0060\ V)$, α' is the forward rate scaled by the fraction of Ca^{2+} bound channels, β is the backward rate of TRPM4 channel closing, $\beta(V) = 0.033 \exp(-0.019\ V)$ and $[Ca^{2+}]_{ND}$ is the Ca^{2+} concentration in the nanodomain. When removing the voltage-dependence of TRPM4 channels, we set V in the equations above to the steady-state value at -60 mV. We injected enough current into the model to hold the membrane potential at -60 mV long enough for all transients to equilibrate before injecting a two second temporally symmetric current

827 ramp in the soma. The amplitude of the ramp was adjusted to reach similar peak frequencies as in the
828 experiments, 10 to 25 Hz.

829 The persistent current during the interspike intervals determines the spike frequency. In order to focus on
830 the rate determining currents in Figures 8 and 9, we removed points from the traces during spiking by
831 eliminating points at which the absolute value of the first temporal derivative of the current trace exceeded
832 0.005 μA/ms·cm^2 for the net current, 0.15 μA/ms·cm^2 for the TRPM4 current, and 0.2 μA/ms·cm^2 for the
833 NaV current. Points outside the range of -0.3 to 0.09 μA/cm^2 in the net current trace, greater than 0 μA/cm^2
834 in the TRPM4 trace and less than -10 μA in the Nav current were also removed. Points were removed from
835 the occupancy in O trace if the absolute value of the first temporal derivative of the O state exceeded
836 0.00002/ms or when occupancy exceeded 0.0002.

837

838 *Software accessibility*

839 Model code is freely available and can be downloaded from ModelDB at: http://modeldb.yale.edu/267599,
840 access code: cholinergicshift.

841

842

843 **REFERENCES**

844 Abbott LF, Blum KI (1996) Functional significance of long-term potentiation for sequence learning and
845 prediction. Cereb Cortex N Y N 1991 6:406–416.

846 Acquas E, Wilson C, Fibiger HC (1996) Conditioned and unconditioned stimuli increase frontal cortical and
847 hippocampal acetylcholine release: effects of novelty, habituation, and fear. J Neurosci Off J Soc Neurosci
848 16:3089–3096.

849 Arboit A, Reboreda A, Yoshida M (2020) Involvement of TRPC4 and 5 Channels in Persistent Firing in
850 Hippocampal CA1 Pyramidal Cells. Cells 9.

851 Ashhad S, Narayanan R (2013) Quantitative interactions between the A-type K^+ current and inositol
852 trisphosphate receptors regulate intraneuronal Ca^{2+} waves and synaptic plasticity: Transient K^+ current
853 regulates ER Ca^{2+} release. J Physiol 591:1645–1669.

854 Autzen HE, Myasnikov AG, Campbell MG, Asarnow D, Julius D, Cheng Y (2018) Structure of the human
855 TRPM4 ion channel in a lipid nanodisc. Science 359:228–232.

856 Avignone E, Cherubini E (1999) Muscarinic receptor modulation of GABA-mediated giant depolarizing
857 potentials in the neonatal rat hippocampus. J Physiol 518:97–107.

858 Aznavour N, Mechawar N, Descarries L (2002) Comparative analysis of cholinergic innervation in the
859 dorsal hippocampus of adult mouse and rat: A quantitative immunocytochemical study. Hippocampus
860 12:206–217.

Azouz R, Jensen MS, Yaari Y (1994) Muscarinic Modulation of Intrinsic Burst Firing in Rat Hippocampal Neurons. Eur J Neurosci 6:961–966.

Balbi P, Massobrio P, Hellgren Kotaleski J (2017) A single Markov-type kinetic model accounting for the macroscopic currents of all human voltage-gated sodium channel isoforms Gillespie D, ed. PLOS Comput Biol 13:e1005737.

Benardo LS, Prince DA (1982) Cholinergic excitation of mammalian hippocampal pyramidal cells. Brain Res 249:315–331.

Bianchi D, Marasco A, Limongiello A, Marchetti C, Marie H, Tirozzi B, Migliore M (2012) On the mechanisms underlying the depolarization block in the spiking dynamics of CA1 pyramidal neurons. J Comput Neurosci 33:207–225.

Bianchi L, Ballini C, Colivicchi MA, Della Corte L, Giovannini MG, Pepeu G (2003) Investigation on Acetylcholine, Aspartate, Glutamate and GABA Extracellular Levels from Ventral Hippocampus During Repeated Exploratory Activity in the Rat. Neurochem Res 28:565–573.

Bittner KC, Grienberger C, Vaidya SP, Milstein AD, Macklin JJ, Suh J, Tonegawa S, Magee JC (2015) Conjunctive input processing drives feature selectivity in hippocampal CA1 neurons. Nat Neurosci 18:1133–1142.

Bittner KC, Milstein AD, Grienberger C, Romani S, Magee JC (2017) Behavioral time scale synaptic plasticity underlies CA1 place fields. Science 357:1033–1036.

Bland BH, Colom LV, Konopacki J, Roth SH (1988) Intracellular records of carbachol-induced theta rhythm in hippocampal slices. Brain Res 447:364–368.

Blum KI, Abbott LF (1996) A model of spatial map formation in the hippocampus of the rat. Neural Comput 8:85–93.

Brown DA, Adams PR (1980) Muscarinic suppression of a novel voltage-sensitive K+ current in a vertebrate neurone. Nature 283:673–676.

Buchanan KA, Petrovic MM, Chamberlain SEL, Marrion NV, Mellor JR (2010) Facilitation of long-term potentiation by muscarinic M(1) receptors is mediated by inhibition of SK channels. Neuron 68:948–963.

Burke SN, Maurer AP, Yang Z, Navratilova Z, Barnes CA (2008) Glutamate receptor-mediated restoration of experience-dependent place field expansion plasticity in aged rats. Behav Neurosci 122:535–548.

Carnevale NT, Hines ML (2006) The NEURON Book. Cambridge University Press.

Chen S, Benninger F, Yaari Y (2014) Role of Small Conductance Ca2+-Activated K+ Channels in Controlling CA1 Pyramidal Cell Excitability. J Neurosci 34:8219–8230.

Cohen J (1977) CHAPTER 1 - The Concepts of Power Analysis. In: Statistical Power Analysis for the Behavioral Sciences (Revised Edition), pp 1–17. Academic Press. Available at: https://www.sciencedirect.com/science/article/pii/B9780121790608500062.

Colino A, Halliwell JV (1993) Carbachol Potentiates Q Current and Activates a Calcium-dependent Non-specific Conductance in Rat Hippocampus In Vitro. Eur J Neurosci 5:1198–1209.

Combe CL, Canavier CC, Gasparini S (2018) Intrinsic Mechanisms of Frequency Selectivity in the Proximal Dendrites of CA1 Pyramidal Neurons. J Neurosci 38:8110–8127.

899 Dani JA, Bertrand D (2007) Nicotinic Acetylcholine Receptors and Nicotinic Cholinergic Mechanisms of
900 the Central Nervous System. Annu Rev Pharmacol Toxicol 47:699–729.

901 Dannenberg H, Young K, Hasselmo M (2017) Modulation of Hippocampal Circuits by Muscarinic and
902 Nicotinic Receptors. Front Neural Circuits 11 Available at:
903 https://www.frontiersin.org/articles/10.3389/fncir.2017.00102 [Accessed July 29, 2022].

904 Dasari S, Gulledge AT (2011) M1 and M4 receptors modulate hippocampal pyramidal neurons. J
905 Neurophysiol 105:779–792.

906 Dasari S, Hill C, Gulledge AT (2017) A unifying hypothesis for M1 muscarinic receptor signalling in
907 pyramidal neurons. J Physiol 595:1711–1723.

908 Dienes C, Hézső T, Kiss DZ, Baranyai D, Kovács ZM, Szabó L, Magyar J, Bányász T, Nánási PP, Horváth
909 B, Gönczi M, Szentandrássy N (2021) Electrophysiological Effects of the Transient Receptor Potential
910 Melastatin 4 Channel Inhibitor (4-Chloro-2-(2-chlorophenoxy)acetamido) Benzoic Acid (CBA) in Canine
911 Left Ventricular Cardiomyocytes. Int J Mol Sci 22:9499.

912 Disney AA, Higley MJ (2020) Diverse Spatiotemporal Scales of Cholinergic Signaling in the Neocortex. J
913 Neurosci 40:720–725.

914 Dong C, Madar AD, Sheffield MEJ (2021) Distinct place cell dynamics in CA1 and CA3 encode experience
915 in new environments. Nat Commun 12:2977.

916 Dutar P, Bassant MH, Senut MC, Lamour Y (1995) The septohippocampal pathway: structure and function
917 of a central cholinergic system. Physiol Rev 75:393–427.

918 Dutta Banik D, Martin LE, Freichel M, Torregrossa A-M, Medler KF (2018) TRPM4 and TRPM5 are both
919 required for normal signaling in taste receptor cells. Proc Natl Acad Sci 115 Available at:
920 https://pnas.org/doi/full/10.1073/pnas.1718802115 [Accessed August 5, 2022].

921 Easton A, Douchamps V, Eacott M, Lever C (2012) A specific role for septohippocampal acetylcholine in
922 memory? Neuropsychologia 50:3156–3168.

923 Egorov AV, Hamam BN, Fransén E, Hasselmo ME, Alonso AA (2002) Graded persistent activity in
924 entorhinal cortex neurons. Nature 420:173–178.

925 Egorov AV, Schumacher D, Medert R, Birnbaumer L, Freichel M, Draguhn A (2019) TRPC channels are
926 not required for graded persistent activity in entorhinal cortex neurons. Hippocampus 29:1038–1048.

927 Ehrlich BE, Kaftan E, Bezprozvannaya S, Bezprozvanny I (1994) The pharmacology of intracellular Ca2+-
928 release channels. Trends Pharmacol Sci 15:145–149.

929 Ekstrom AD, Meltzer J, McNaughton BL, Barnes CA (2001) NMDA Receptor Antagonism Blocks
930 Experience-Dependent Expansion of Hippocampal “Place Fields.” Neuron 31:631–638.

931 Epsztein J, Brecht M, Lee AK (2011) Intracellular Determinants of Hippocampal CA1 Place and Silent Cell
932 Activity in a Novel Environment. Neuron 70:109–120.

933 Fakler B, Adelman JP (2008) Control of K(Ca) channels by calcium nano/microdomains. Neuron 59:873–
934 881.

935 Fernández de Sevilla D, Núñez A, Buño W (2021) Muscarinic Receptors, from Synaptic Plasticity to its
936 Role in Network Activity. Neuroscience 456:60–70.

937 Fernandez FR, White JA (2010) Gain Control in CA1 Pyramidal Cells Using Changes in Somatic
938 Conductance. J Neurosci 30:230–241.

939 Fisahn A, Pike FG, Buhl EH, Paulsen O (1998) Cholinergic induction of network oscillations at 40 Hz in
940 the hippocampus in vitro. Nature 394:186–189.

941 Frank D, Kafkas A (2021) Expectation-driven novelty effects in episodic memory. Neurobiol Learn Mem
942 183:107466.

943 Fraser DD, MacVicar BA (1996) Cholinergic-Dependent Plateau Potential in Hippocampal CA1 Pyramidal
944 Neurons. J Neurosci 16:4113–4128.

945 Gafni J, Munsch JA, Lam TH, Catlin MC, Costa LG, Molinski TF, Pessah IN (1997) Xestospongins: potent
946 membrane permeable blockers of the inositol 1,4,5-trisphosphate receptor. Neuron 19:723–733.

947 Gasparini S, Magee JC (2002) Phosphorylation-dependent differences in the activation properties of distal
948 and proximal dendritic Na+ channels in rat CA1 hippocampal neurons. J Physiol 541:665–672.

949 Gasparini S, Migliore M (2015) Action Potential Backpropagation. In: Encyclopedia of Computational
950 Neuroscience (Jaeger D, Jung R, eds), pp 133–137. New York, NY: Springer. Available at:
951 https://doi.org/10.1007/978-1-4614-6675-8_123 [Accessed August 18, 2021].

952 Giessel AJ, Sabatini BL (2010) M1 Muscarinic Receptors Boost Synaptic Potentials and Calcium Influx in
953 Dendritic Spines by Inhibiting Postsynaptic SK Channels. Neuron 68:936–947.

954 Giovannini MG, Rakovska A, Benton RS, Pazzagli M, Bianchi L, Pepeu G (2001) Effects of novelty and
955 habituation on acetylcholine, GABA, and glutamate release from the frontal cortex and hippocampus of
956 freely moving rats. Neuroscience 106:43–53.

957 Gómez-Ocádiz R, Trippa M, Zhang C-L, Posani L, Cocco S, Monasson R, Schmidt-Hieber C (2022) A
958 synaptic signal for novelty processing in the hippocampus. Nat Commun 13.

959 Gonzales AL, Amberg GC, Earley S (2010) Ca^{2+} release from the sarcoplasmic reticulum is required for
960 sustained TRPM4 activity in cerebral artery smooth muscle cells. Am J Physiol-Cell Physiol 299:C279–
961 C288.

962 Gonzales AL, Earley S (2012) Endogenous cytosolic Ca2+ buffering is necessary for TRPM4 activity in
963 cerebral artery smooth muscle cells. Cell Calcium 51:82–93.

964 Guinamard R, Demion M, Launay P (2010) Physiological Roles of the TRPM4 Channel Extracted from
965 Background Currents. Physiology 25:155–164.

966 Guinamard R, Simard C, Del Negro C (2013) Flufenamic acid as an ion channel modulator. Pharmacol
967 Ther 138:272–284.

968 Halliwell JV, Adams PR (1982) Voltage-clamp analysis of muscarinic excitation in hippocampal neurons.
969 Brain Res 250:71–92.

970 Hargreaves EL, Yoganarasimha D, Knierim JJ (2007) Cohesiveness of spatial and directional
971 representations recorded from neural ensembles in the anterior thalamus, parasubiculum, medial
972 entorhinal cortex, and hippocampus. Hippocampus 17:826–841.

973 Harney SC, Rowan M, Anwyl R (2006) Long-Term Depression of NMDA Receptor-Mediated Synaptic
974 Transmission Is Dependent on Activation of Metabotropic Glutamate Receptors and Is Altered to Long-
975 Term Potentiation by Low Intracellular Calcium Buffering. J Neurosci 26:1128–1132.

976 Harvey CD, Collman F, Dombeck DA, Tank DW (2009) Intracellular dynamics of hippocampal place cells
977 during virtual navigation. Nature 461:941–946.

978 Hasselmo ME (2006) The role of acetylcholine in learning and memory. Curr Opin Neurobiol 16:710–715.

979 Hines ML, Carnevale NT (1997) The NEURON simulation environment. Neural Comput 9:1179–1209.

980 Hoffman DA, Johnston D (1998) Downregulation of Transient K+ Channels in Dendrites of Hippocampal
981 CA1 Pyramidal Neurons by Activation of PKA and PKC. J Neurosci 18:3521–3528.

982 Hoffman DA, Magee JC, Colbert CM, Johnston D (1997) K+ channel regulation of signal propagation in
983 dendrites of hippocampal pyramidal neurons. Nature 387:869–875.

984 Hofmann T, Obukhov AG, Schaefer M, Harteneck C, Gudermann T, Schultz G (1999) Direct activation of
985 human TRPC6 and TRPC3 channels by diacylglycerol. Nature 397:259–263.

986 Hou J, Fei Y, Li W, Chen Y, Wang Q, Xiao Y, Wang Y, Li Y (2018) The transient receptor potential
987 melastatin 4 channel inhibitor 9-phenanthrol modulates cardiac sodium channel: 9-Phenanthrol inhibits
988 cardiac sodium channel. Br J Pharmacol 175:4325–4337.

989 Hsu C-L, Zhao X, Milstein AD, Spruston N (2018) Persistent Sodium Current Mediates the Steep Voltage
990 Dependence of Spatial Coding in Hippocampal Pyramidal Neurons. Neuron 99:147-162.e8.

991 Huerta PT, Lisman JE (1995) Bidirectional synaptic plasticity induced by a single burst during cholinergic
992 theta oscillation in CA1 in vitro. Neuron 15:1053–1063.

993 Huff AE, McGraw SD, Winters BD (2022) Muscarinic (M1) cholinergic receptor activation within the dorsal
994 hippocampus promotes destabilization of strongly encoded object location memories. Hippocampus
995 32:55–66.

996 Hutchison IC, Rathore S (2015) The role of REM sleep theta activity in emotional memory. Front Psychol
997 6 Available at: http://journal.frontiersin.org/article/10.3389/fpsyg.2015.01439 [Accessed August 26, 2022].

998 Isokawa M, Alger BE (2006) Ryanodine Receptor Regulates Endogenous Cannabinoid Mobilization in the
999 Hippocampus. J Neurophysiol 95:3001–3011.

000 Knauer B, Jochems A, Valero-Aracama MJ, Yoshida M (2013) Long-lasting intrinsic persistent firing in rat
001 CA1 pyramidal cells: A possible mechanism for active maintenance of memory: Long-Lasting Persistent
002 Firing in Ca1 Pyramidal Cells. Hippocampus 23:820–831.

003 Kopsick JD, Hartzell K, Lazaro H, Nambiar P, Hasselmo ME, Dannenberg H (2022) Temporal dynamics
004 of cholinergic activity in the septo-hippocampal system. Front Neural Circuits 16:957441.

005 Launay P, Fleig A, Perraud A-L, Scharenberg AM, Penner R, Kinet J-P (2002) TRPM4 Is a Ca2+-Activated
006 Nonselective Cation Channel Mediating Cell Membrane Depolarization. Cell 109:397–407.

007 Lee I, Griffin AL, Zilli EA, Eichenbaum H, Hasselmo ME (2006) Gradual translocation of spatial correlates
008 of neuronal firing in the hippocampus toward prospective reward locations. Neuron 51:639–650.

009 Lei Y-T, Thuault SJ, Launay P, Margolskee RF, Kandel ER, Siegelbaum SA (2014) Differential contribution
010 of TRPM4 and TRPM5 nonselective cation channels to the slow afterdepolarization in mouse prefrontal
011 cortex neurons. Front Cell Neurosci 8 Available at:
012 http://journal.frontiersin.org/article/10.3389/fncel.2014.00267/abstract.

013 Levey A, Edmunds S, Koliatsos V, Wiley R, Heilman C (1995) Expression of m1-m4 muscarinic
014 acetylcholine receptor proteins in rat hippocampus and regulation by cholinergic innervation. J Neurosci
015 15:4077–4092.

016 Li K, Abbott SBG, Shi Y, Eggan P, Gonye EC, Bayliss DA (2021) TRPM4 mediates a subthreshold
017 membrane potential oscillation in respiratory chemoreceptor neurons that drives pacemaker firing and
018 breathing. Cell Rep 34:108714.

019 Lin EC, Combe CL, Gasparini S (2017) Differential Contribution of Ca2+-Dependent Mechanisms to
020 Hyperexcitability in Layer V Neurons of the Medial Entorhinal Cortex. Front Cell Neurosci 11:182.

021 Losonczy A, Makara JK, Magee JC (2008) Compartmentalized dendritic plasticity and input feature storage
022 in neurons. Nature 452:436–441.

023 Magee JC (1998) Dendritic Hyperpolarization-Activated Currents Modify the Integrative Properties of
024 Hippocampal CA1 Pyramidal Neurons. J Neurosci 18:7613–7624.

025 Mainen ZF, Sejnowski TJ (1995) Reliability of Spike Timing in Neocortical Neurons. Science 268:1503–
026 1506.

027 Martina M, Schultz JH, Ehmke H, Monyer H, Jonas P (1998) Functional and Molecular Differences
028 between Voltage-Gated K^+ Channels of Fast-Spiking Interneurons and Pyramidal Neurons of Rat
029 Hippocampus. J Neurosci 18:8111–8125.

030 Masoli S, Tognolina M, Laforenza U, Moccia F, D'Angelo E (2020) Parameter tuning differentiates granule
031 cell subtypes enriching transmission properties at the cerebellum input stage. Commun Biol 3:222.

032 Mederos Y Schnitzler M, Gudermann T, Storch U (2018) Emerging Roles of Diacylglycerol-Sensitive
033 TRPC4/5 Channels. Cells 7.

034 Megías M, Emri Z, Freund TF, Gulyás AI (2001) Total number and distribution of inhibitory and excitatory
035 synapses on hippocampal CA1 pyramidal cells. Neuroscience 102:527–540.

036 Mehta MR, Quirk MC, Wilson MA (2000) Experience-Dependent Asymmetric Shape of Hippocampal
037 Receptive Fields. Neuron 25:707–715.

038 Menigoz A, Ahmed T, Sabanov V, Philippaert K, Pinto S, Kerselaers S, Segal A, Freichel M, Voets T, Nilius
039 B, Vennekens R, Balschun D (2016) TRPM4-dependent post-synaptic depolarization is essential for the
040 induction of NMDA receptor-dependent LTP in CA1 hippocampal neurons. Pflüg Arch - Eur J Physiol
041 468:593–607.

042 Micheau J, Marighetto A (2011) Acetylcholine and memory: A long, complex and chaotic but still living
043 relationship. Behav Brain Res 221:424–429.

044 Mickus T, Jung H, Spruston N (1999) Properties of Slow, Cumulative Sodium Channel Inactivation in Rat
045 Hippocampal CA1 Pyramidal Neurons. Biophys J 76:846–860.

046 Mironov SL (2008) Metabotropic glutamate receptors activate dendritic calcium waves and TRPM channels
047 which drive rhythmic respiratory patterns in mice: mGluR, TRPM4 channels, calcium waves and inspiratory
048 bursts. J Physiol 586:2277–2291.

049 Nilius B, Mahieu F, Prenen J, Janssens A, Owsianik G, Vennekens R, Voets T (2006) The Ca2+-activated
050 cation channel TRPM4 is regulated by phosphatidylinositol 4,5-biphosphate. EMBO J 25:467–478.

051 Nilius B, Prenen J, Droogmans G, Voets T, Vennekens R, Freichel M, Wissenbach U, Flockerzi V (2003)
052 Voltage dependence of the Ca2+-activated cation channel TRPM4. J Biol Chem 278:30813–30820.

053 Nilius B, Prenen J, Janssens A, Voets T, Droogmans G (2004) Decavanadate modulates gating of TRPM4
054 cation channels: Decavanadate modulates TRPM4. J Physiol 560:753–765.

055 Nilius B, Prenen J, Tang J, Wang C, Owsianik G, Janssens A, Voets T, Zhu MX (2005) Regulation of the
056 Ca2+ Sensitivity of the Nonselective Cation Channel TRPM4*. J Biol Chem 280:6423–6433.

057 Nyakas C, Luiten PGM, Spencer DG, Traber J (1987) Detailed projection patterns of septal and diagonal
058 band efferents to the hippocampus in the rat with emphasis on innervation of CA1 and dentate gyrus. Brain
059 Res Bull 18:533–545.

060 O'Malley JJ, Seibt F, Chin J, Beierlein M (2020) TRPM4 Conductances in Thalamic Reticular Nucleus
061 Neurons Generate Persistent Firing during Slow Oscillations. J Neurosci 40:4813–4823.

062 Pace RW, Mackay DD, Feldman JL, Del Negro CA (2007) Inspiratory bursts in the preBötzinger complex
063 depend on a calcium-activated non-specific cation current linked to glutamate receptors in neonatal mice:
064 Inspiratory drive potential mechanisms in preBötC neurons. J Physiol 582:113–125.

065 Palacios-Filardo J, Mellor JR (2019) Neuromodulation of hippocampal long-term synaptic plasticity. Curr
066 Opin Neurobiol 54:37–43.

067 Palacios-Filardo J, Udakis M, Brown GA, Tehan BG, Congreve MS, Nathan PJ, Brown AJH, Mellor JR
068 (2021) Acetylcholine prioritises direct synaptic inputs from entorhinal cortex to CA1 by differential
069 modulation of feedforward inhibitory circuits. Nat Commun 12:5475.

070 Partridge LD, Valenzuela CF (2000) Block of hippocampal CAN channels by flufenamate. Brain Res
071 867:143–148.

072 Pepeu G, Giovannini MG (2004) Changes in Acetylcholine Extracellular Levels During Cognitive
073 Processes: Table 1. Learn Mem 11:21–27.

074 Picardo MCD, Sugimura YK, Dorst KE, Kallurkar PS, Akins VT, Ma X, Teruyama R, Guinamard R, Kam
075 K, Saha MS, Del Negro CA (2019) Trpm4 ion channels in pre-Bötzinger complex interneurons are essential
076 for breathing motor pattern but not rhythm Dubuc R, ed. PLOS Biol 17:e2006094.

077 Poirazi P, Brannon T, Mel BW (2003a) Arithmetic of subthreshold synaptic summation in a model CA1
078 pyramidal cell. Neuron 37:977–987.

079 Poirazi P, Brannon T, Mel BW (2003b) Pyramidal Neuron as Two-Layer Neural Network. Neuron 37:989–
080 999.

081 Priestley JB, Bowler JC, Rolotti SV, Fusi S, Losonczy A (2022) Signatures of rapid plasticity in hippocampal
082 CA1 representations during novel experiences. Neuron 110:1978-1992.e6.

083 Provence A, Rovner ES, Petkov GV (2017) Regulation of transient receptor potential melastatin 4 channel
084 by sarcoplasmic reticulum inositol trisphosphate receptors: Role in human detrusor smooth muscle
085 function. Channels Austin Tex 11:459–466.

086 Putney JW (2005) Physiological mechanisms of TRPC activation. Pflüg Arch - Eur J Physiol 451:29–34.

087 Raymond CR, Redman SJ (2006) Spatial segregation of neuronal calcium signals encodes different forms
088 of LTP in rat hippocampus. J Physiol 570:97–111.

Reboreda A, Jiménez-Díaz L, Navarro-López JD (2011) TRP Channels and Neural Persistent Activity. In: Transient Receptor Potential Channels (Islam MdS, ed), pp 595–613 Advances in Experimental Medicine and Biology. Dordrecht: Springer Netherlands. Available at: http://link.springer.com/10.1007/978-94-007-0265-3_32 [Accessed August 9, 2022].

Resnik E, McFarland JM, Sprengel R, Sakmann B, Mehta MR (2012) The effects of GluA1 deletion on the hippocampal population code for position. J Neurosci Off J Soc Neurosci 32:8952–8968.

Riquelme D, Cerda O, Leiva-Salcedo E (2021) TRPM4 Expression During Postnatal Developmental of Mouse CA1 Pyramidal Neurons. Front Neuroanat 15:643287.

Roth ED, Yu X, Rao G, Knierim JJ (2012) Functional Differences in the Backward Shifts of CA1 and CA3 Place Fields in Novel and Familiar Environments Gilestro GF, ed. PLoS ONE 7:e36035.

Sahu G, Turner RW (2021) The Molecular Basis for the Calcium-Dependent Slow Afterhyperpolarization in CA1 Hippocampal Pyramidal Neurons. Front Physiol 12 Available at: https://www.frontiersin.org/articles/10.3389/fphys.2021.759707.

Sarter M, Lustig C (2020) Forebrain Cholinergic Signaling: Wired and Phasic, Not Tonic, and Causing Behavior. J Neurosci 40:712–719.

Savelli F, Knierim JJ (2010) Hebbian analysis of the transformation of medial entorhinal grid-cell inputs to hippocampal place fields. J Neurophysiol 103:3167–3183.

Shah MM, Migliore M, Valencia I, Cooper EC, Brown DA (2008) Functional significance of axonal Kv7 channels in hippocampal pyramidal neurons. Proc Natl Acad Sci 105:7869–7874.

Simard C, Sallé L, Rouet R, Guinamard R (2012) Transient receptor potential melastatin 4 inhibitor 9-phenanthrol abolishes arrhythmias induced by hypoxia and re-oxygenation in mouse ventricle: Anti-arrhythmic effect of 9-phenanthrol. Br J Pharmacol 165:2354–2364.

Takács VT, Cserép C, Schlingloff D, Pósfai B, Szőnyi A, Sos KE, Környei Z, Dénes Á, Gulyás AI, Freund TF, Nyiri G (2018) Co-transmission of acetylcholine and GABA regulates hippocampal states. Nat Commun 9:2848.

Tedoldi A, Ludwig P, Fulgenzi G, Takeshima H, Pedarzani P, Stocker M (2020) Calcium-induced calcium release and type 3 ryanodine receptors modulate the slow afterhyperpolarising current, sIAHP, and its potentiation in hippocampal pyramidal neurons. PLOS ONE 15:e0230465.

Thiel CM, Huston JP, Schwarting RKW (1998) Hippocampal acetylcholine and habituation learning. Neuroscience 85:1253–1262.

Upchurch CM, Combe CL, Knowlton CJ, Rousseau VG, Gasparini S, Canavier CC (2022) Long-Term Inactivation of Sodium Channels as a Mechanism of Adaptation in CA1 Pyramidal Neurons. J Neurosci 42:3768–3782.

Venkatesan K, Liu Y, Goldfarb M (2014) Fast-Onset Long-Term Open-State Block of Sodium Channels by A-type FHFs Mediates Classical Spike Accommodation in Hippocampal Pyramidal Neurons. J Neurosci 34:16126–16139.

Venugopal S, Hsiao C-F, Sonoda T, Wiedau-Pazos M, Chandler SH (2015) Homeostatic dysregulation in membrane properties of masticatory motoneurons compared with oculomotor neurons in a mouse model for amyotrophic lateral sclerosis. J Neurosci Off J Soc Neurosci 35:707–720.

128 Veress R, Baranyai D, Hegyi B, Kistamás K, Dienes C, Magyar J, Bányász T, Nánási PP, Szentandrássy
129 N, Horváth B (2018) Transient receptor potential melastatin 4 channel inhibitor 9-phenanthrol inhibits K^+
130 but not Ca^{2+} currents in canine ventricular myocytes. Can J Physiol Pharmacol 96:1022–1029.

131 Vierra NC, Kirmiz M, van der List D, Santana LF, Trimmer JS (2019) Kv2.1 mediates spatial and functional
132 coupling of L-type calcium channels and ryanodine receptors in mammalian neurons Swartz KJ, Marder
133 E, eds. eLife 8:e49953.

134 Yamada-Hanff J, Bean BP (2013) Persistent sodium current drives conditional pacemaking in CA1
135 pyramidal neurons under muscarinic stimulation. J Neurosci 33:15011–15021.

136 Yamasaki M, Matsui M, Watanabe M (2010) Preferential Localization of Muscarinic M1 Receptor on
137 Dendritic Shaft and Spine of Cortical Pyramidal Cells and Its Anatomical Evidence for Volume
138 Transmission. J Neurosci 30:4408–4418.

139 Yoshida M, Knauer B, Jochems A (2012) Cholinergic modulation of the CAN current may adjust neural
140 dynamics for active memory maintenance, spatial navigation and time-compressed replay. Front Neural
141 Circuits 6 Available at: http://journal.frontiersin.org/article/10.3389/fncir.2012.00010/abstract.

142 Zhang Z, Reboreda A, Alonso A, Barker PA, Séguéla P (2011) TRPC channels underlie cholinergic plateau
143 potentials and persistent activity in entorhinal cortex. Hippocampus 21:386–397.

144 Zhu MX (2005) Multiple roles of calmodulin and other Ca2+-binding proteins in the functional regulation of
145 TRP channels. Pflüg Arch - Eur J Physiol 451:105–115.

146

147 **Figure legends**

148 Figure 1. Carbachol shifts the center of mass of firing in response to depolarizing current ramps.
149 A. Somatic recording, control. A1. Voltage trace for a two second triangular current ramp (represented
150 below) injected in the soma. A2. Instantaneous frequency for example in A1 as it changes along the ramp.
151 A3. Raster plot of different trials recorded from the same example neuron in A1. The trials are ordered by
152 the amplitude of the peak injected current, from lowest (bottom) to highest (top); trials with the same
153 amount of current injection are clustered together. B. Somatic recording, carbachol. B1, B2, and B3. Same
154 as A1, A2, and A3, but during superfusion with 2 μM CCh. C1. Instantaneous frequency for example in A1,
155 as it changes with injected current. Filled circles represent firing on the up-ramp; open circles, firing on the
156 down-ramp. C2. Instantaneous frequency for example in B1. A, B, and C are recordings from the same
157 cell. D. Summary data of the adaptation index for somatic recordings, before and during CCh, for two
158 second ramps (n = 21) and ten second ramps (n = 19). Open circles connected by gray lines represent
159 indices for individual cells, before and during CCh. Black squares with error bars represent group averages
160 ± SEM. In control, all adaptation indices are positive, indicating more action potentials on the up-ramp. In
161 CCh, most adaptation indices are negative, indicating more action potentials on the down-ramp. E.
162 Dendritic recording, control. E1. Voltage trace for a two second triangular current ramp (represented below)
163 injected in the dendrite, approximately 200 μm from the soma. E2. Instantaneous frequency for E1 as it
164 changes along the ramp. E3. Raster plot of different trials recorded from same example neuron in E1. F.
165 Dendritic recording, carbachol. F1, F2, and F3. Same as E1, E2, and E3, but during superfusion with 2 μM

166 CCh. G1. Instantaneous frequency for example in E1, as it changes with injected current. G2.
167 Instantaneous frequency for example in F1. E, F, and G are from the same cell. H. Summary data of the
168 adaptation index for dendritic ramps, before and during CCh, for two second ramps (n = 19) and ten second
169 ramps (n = 10). *** $p < 0.0005$. Red dotted lines in the left panels mark the middle of the current injection
170 ramp. Source data in "Figure 1 - Source data". See also Figure 1 – supplement 1 and Figure 1 –
171 supplement 2.
172
173 Figure 2. Cholinergic modulation of the response to electrical stimulation of Schaffer collaterals, recorded
174 at the soma. A Top, synaptic response in control conditions to an input frequency that increases and
175 decreases symmetrically, from 6.7 to 25 Hz, as denoted by the pulses under the voltage trace. Bottom,
176 Raster plot of multiple trials repeated at the same stimulation intensity. B same as A during superfusion of
177 2 μM CCh. A and B are from the same neuron, and at the same stimulation intensity. Diamonds in A and
178 B point to a longer EPSP decay time in the presence of CCh. C. Summary data of the adaptation index for
179 synaptic ramps, before and during CCh. D. Summary data of the average EPSP amplitude measured
180 during trials where the cells did not fire in response to the first stimulus pulse, before and during CCh. In
181 both cases, open circles connected by gray lines represent indices for individual cells; black squares with
182 error bars represent group averages ± SEM *** $p < 0.0005$, ** $p = 0.002$. Red dotted lines in the panels on
183 the left mark the middle of the synaptic stimulation. Source data in "Figure 2 - Source data".
184
185 Figure 3. Modulation of response to symmetric ramps by acetylcholine is concentration dependent.
186 A. Voltage trace recorded in the soma for a two second triangular current ramp injected in the soma in
187 control. Current traces and instantaneous frequency plots are just below the voltage traces. B-D. Same as
188 A, during superfusion with 2 μM ACh (B), 10 μM ACh (C), and 15 μM ACh (D). A through D are from the
189 same cell. E. Summary data of the adaptation index for control and the three concentrations of ACh,
190 applied in order of increasing concentration (n = 13). Open circles connected by gray lines represent
191 indices for individual cells over all four conditions. Black squares with error bars represent group averages
192 ± SEM. *** $p < 0.0005$, ** $p = 0.001$, * $p = 0.01$. Red dotted lines in the panels on the left mark the middle
193 of the current injection ramp. Source data in "Figure 3 - Source data".
194
195 Figure 4. Cholinergic-associated shift in the timing of firing on ramp is mediated by TRP channels, but
196 notably not TRPC channels. A. Somatic recordings for a two second triangular current ramp injected in the
197 soma in control (A1), CCh (2 μM, A2), and CCh + FFA (100 μM, A3) applied subsequently to the same
198 cell. Current traces and instantaneous frequency plots are just below the voltage traces. Summary data
199 (A4) of the adaptation index for control, CCh, and CCh + FFA (n = 9). B. Same as in A, but for dendritic
200 injection and recordings. Summary data (B4) of the adaptation index for control, CCh, and CCh + FFA (n
201 = 9). Open circles connected by gray lines represent indices for individual cells, over all three treatments.

202 Black squares with error bars represent group averages ± SEM. C. Somatic recordings for a two second
203 triangular current ramp injected in the soma in control (C1), CCh (2 μM, C2), and CCh + SKF96365 (50
204 μM, C3) applied subsequently to the same cell. Current traces and instantaneous frequency plots are just
205 below voltage traces. Red dotted line marks the middle of the ramp. Summary data (C4) of the adaptation
206 index for control, CCh, and CCh + SKF96365 (n = 8). D. Same as in C, but for dendritic injection and
207 recordings. Summary data (D4) of the adaptation index for control, CCh, and CCh + SKF96365 (n = 8). ***
208 p < 0.0005, ** p = 0.001, * p = 0.02, n.s. not significant. Source data in "Figure 4 - Source data".
209
210 Figure 5. Cholinergic-mediated shift in the center of mass of firing is mediated by TRPM4 channels.
211 A. Somatic recordings for a two second triangular current ramp injected in the soma in control (A1), CCh
212 (2 μM, A2), and CCh + CBA (50 μM, A3) applied subsequently to the same cell. Current traces and
213 instantaneous frequency plots are just below voltage traces. Red dotted line marks the middle of the ramp.
214 Summary data (A4) of the adaptation index for control, CCh, and CCh + CBA (n = 9). Open circles
215 connected by gray lines represent indices for individual cells, over all three treatments. Black squares with
216 error bars represent group averages ± SEM. B. Same as in A, but for dendritic injection and recordings.
217 Summary data (B4) of the adaptation index for control, CCh, and CCh + CBA (n = 9). C. Same as A, but
218 for control (C1), CCh (2 μM, C2), and CCh + 9-phenanthrol (100 μM, C3) applied subsequently to the same
219 cell. Summary data (C4) of the adaptation index for control, CCh, and CCh + 9-phenanthrol (n = 8). *** p
220 < 0.0005, ** p = 0.002, * p = 0.02, ## p = 0.001, # p = 0.03, n.s. not significant. Source data in "Figure 5 -
221 Source data".
222
223 Figure 6. Pharmacological block of IP_3R or RyRs has no effect on CCh-mediated shift in firing along ramp.
224 A. Somatic recordings during intracellular dialysis with Xestospongin C (2 μM), for a two second triangular
225 current ramp injected in the soma before (A1), and during superfusion with CCh (2 μM, A2). Current traces
226 and instantaneous frequency plots are just below voltage traces. Summary data (A3) of the adaptation
227 index for Xestospongin C (1-2 μM) and CCh (n = 9). Circles connected by gray lines represent ratios for
228 individual cells, before and during CCh. Filled circles represent cells dialyzed with 1 μM Xestospongin C
229 and open circles represent cells dialyzed with 2 μM Xestospongin C. Black squares with error bars
230 represent group averages ± SEM. B. Same as A, but intracellular dialysis is with ryanodine (40 μM).
231 Summary data (B3) of the adaptation index for ryanodine and CCh (n = 9). Individual cells represented by
232 open circles. *** p < 0.0005. In both sets of experiments, control data reflect the effect of either IP_3R or
233 RyR antagonist before the addition of CCh, because the dialysis started to be apparent quickly after break-
234 in. Red dotted lines in the left panels mark the middle of the ramp. C1 and C2. Same as B1 and B2; C3 is
235 an expanded version of the inset in C1. Source data in "Figure 6 - Source data".
236

237 Figure 7. A. Simulated control response to triangular current ramp. A1. Top. Simplified model calcium
238 handling schematic. For simplicity, only one annulus (shell) is shown, and the rest are represented as the
239 core. Ca^{2+} enters via voltage-gated Ca^{2+} channels (Ca_V) and is removed by the plasma membrane Ca^{2+}
240 ATPase (PMCA) pump. Inside the cell, buffering and the endoplasmic reticulum (ER) are also modeled.
241 The TRPM4 channel is not permeable to Ca^{2+} and senses [Ca^{2+}] in a nanodomain (ND). In the control
242 simulation, the nanodomain is contiguous with the cytosol. Bottom trace shows the voltage responses,
243 plotted in the somatic compartment, to a triangular current ramp applied in the soma (shown below). A2.
244 Ca^{2+} concentration (in nM) in the outermost shell of the somatic compartment. A3. The nanodomain Ca^{2+}
245 concentration (same as the that of the outer shell in A2 in this case) is negligible when plotted in μM scale.
246 A4. TRPM4 activation is negligible in control. B. Simulated response to triangular current ramp during
247 simulated application of CCh. B1. As in A1 except for ligand (magenta dot) binding to the metabotropic
248 acetylcholine receptor (mAChR), triggering Ca^{2+} influx into a nanodomain linked to the TRPM4 channel.
249 The voltage trace shows that the center of mass of firing is shifted to later times. B2. Ca^{2+} concentration
250 (in nM) in the outermost shell of the somatic compartment. B3. In contrast to control, the addition of a
251 nanodomain with privileged Ca^{2+} access allows micromolar concentrations to be reached and sensed by
252 TRPM4 channels. B4. In contrast to control, TRPM4 is now activated during the ramp. Vertical dashed red
253 line shows the peak of the current ramp.
254
255 Figure 8. The model explains how simulated TRPM4 channel activation can reverse the adaptation
256 mediated by long-term inactivation of $Na_V1.6$ channels. A. Voltage traces from 7A1 and B1 overlaid; control
257 (in black), CCh (in magenta). The triangular current injection ramps are shown below. B. Occupancy of
258 $Na_V1.6$ channel in the open state (O) in the somatic compartment, with values during spikes removed. C.
259 Occupancy of $Na_V1.6$ channel in the long-term inactivated state (I2). D. Persistent Na_V current (spiking
260 values removed) E. TRPM4 current. F. Net ionic current. All values are shown for somatic compartment.
261
262 Figure 9. The model explains how activation of TRPM4 channels affects the firing pattern in response to
263 triangular ramps that evoke similar firing frequencies. A. Simulated voltage traces (top) during a two second
264 triangular current ramp (just below voltage traces). Insets show the reciprocal of the interspike interval (ISI)
265 plotted as the instantaneous frequency at the ISI midpoint. Vertical dashed red line shows the peak of the
266 current ramp. The slower frequencies at similar values of injected current and fewer ISIs on the down-
267 ramp (open circles) versus the up-ramp (closed circles) in control show hysteresis due to adaptation
268 mediated by long-term inactivation of the sodium channel. TRPM4 channel activation causes the center of
269 mass of firing to be shifted to the right in all other traces compared to control because a nanodomain for
270 TRPM4 activation with special access to Ca^{2+} was added in simulated CCh. The hysteresis is in the
271 opposite direction because the activation of TRPM4 channels by Ca^{2+} accumulation obscures and
272 overwhelms adaptation. In the light blue traces, the voltage-dependence of TRPM4 activation was not

included, so there is less Ca^{2+} accumulation in the outer shell in B and in the nanodomain in C, resulting in less activation of TRPM4 channels in D. In order to isolate the effect of voltage-dependence from that of Ca^{2+} dependence, the Ca^{2+} waveforms in all nanodomains were recorded during the full CCh simulation shown in magenta, and played back into each nanodomain Ca^{2+} during the simulations shown in purple.

Figure 10. A high concentration of BAPTA is required to interfere with CCh-mediated shift in firing along ramp.

A. Somatic recordings during intracellular dialysis with 10 mM BAPTA, for a two second triangular current ramp injected in the soma before (A1), and during superfusion with CCh (2 μM, A2). Current traces and instantaneous frequency plots are just below voltage traces. Red dotted line marks the middle of the ramp. Summary data (A3) of the adaptation index for control and CCh (n = 10). Open circles connected by gray lines represent ratios for individual cells, before and during CCh. Black squares with error bars represent group averages ± SEM. B. Same as A, but intracellular dialysis is with 30 mM BAPTA and 100 nM free [Ca^{2+}]. Summary data (B3) of the adaptation index for control and CCh (n = 8). C. Same as A, but intracellular dialysis is with 30 mM BAPTA and 10 nM free [Ca^{2+}]. Summary data (C3) of the adaptation index for control and CCh (n = 12). *** $p < 0.0005$, ** $p = 0.001$, n.s. not significant. Source data in "Figure 10 - Source data".

Figure 11. Model Schematics.

A. Reconstructed morphology ported to NEURON simulation program, with somatic and dendritic current injection sites labeled. B. Equivalent circuit diagram, with the reversal potentials for each channel indicated by E_X. The following currents were modeled using Ohmic drive and conductances in parallel with a membrane capacitance (C_M): a Na^+ current (I_{Na}), L-type (I_{CaL}), R-type (I_{CaR}), and T-type (I_{CaT}) Ca^{2+} currents, two delayed rectifiers (I_{Kv1} and I_{Kv2}), an A-type K^+ current (I_A), an inward rectifying K^+ current (I_{KIR}), a nonspecific Ca^{2+}-activated current (I_{CAN}), a hyperpolarization-activated mixed cationic h-current (I_h), and a leak current (I_L). C. Markov Model of the NaV channel with an open state (O), a closed state (C), a short-term inactivated state (I1) and a long-term inactivated state (I2). See also Figure 11 – supplement 1.

Figure 1 – supplement 1. Plots of instantaneous frequency versus current injection showing different effects of carbachol on firing rate adaptation. A and B. Two examples of somatic recordings where the firing rate adaptation in control is reversed in the presence of CCh, such that the clockwise hysteresis becomes counter-clockwise. C and D. Two examples of somatic recordings where the firing rate adaptation in control is removed in the presence of CCh, such that the hysteresis disappears, and the motion becomes linear. Filled circles represent the firing frequencies on the up-ramp and open circles represent firing frequencies on the down-ramp.

308

309 Figure 1 – supplement 2. A. Adaptation index as a function of membrane potential. Index values for each
310 trial for all neurons are plotted against the membrane potential measured just before the current injection
311 ramp for that trial, both for somatic recordings (n = 132 in control conditions, filled circles; n = 144 in the
312 presence of CCh 2 μM, open circles) and for dendritic recordings (n = 135 in control conditions, filled
313 circles; n = 87 during CCh, open circles). B. Adaptation index as a function of the peak injected current.
314 Index values for each trial for all recorded neurons are shown plotted against the peak amplitude of the
315 triangular-shaped current injection for that trial, for both somatic and dendritic recordings (values for n and
316 symbols are the same as in A). C. Adaptation index as a function of input resistance. Average adaptation
317 index values per cell for both somatic recordings (n = 17) and dendritic recordings (n = 12) are plotted
318 against the average steady state input resistance measured during control conditions (filled circles) and
319 during perfusion with CCh (open circles). Source data in "Figure 1 supplement 2 - Source data".

320

321 Figure 11 – supplement 1. Old model in which the source of Ca2+ with privileged access to the nanodomain
322 required to activated TRPM4 channels is IP_3R. This model captures the responses seen with cholinergic
323 activation in the experiments. A. Simulated somatic recordings in control (low IP_3). A1. Voltage traces and
324 current ramp. A2. Nanomolar Ca^{2+} concentration in outer shell beneath the cell membrane. A3. The
325 nanodomain Ca^{2+} concentration is not elevated with low levels of IP_3 that simulate control. A4. There is
326 negligible TRPM4 activation. B. Simulated somatic recordings in CCh (high IP_3). B1. Voltage traces and
327 current ramp. B2. Nanomolar Ca^{2+} concentration in outer shell beneath the cell membrane is elevated due
328 to increased spiking on the down-ramp. B3. The nanodomain Ca^{2+} concentration reached micromolar
329 concentrations with high levels of IP_3 that simulate application of CCh. B4. TRPM4 is robustly activated.
330 Black dashed line marks the end of the injected current ramp, highlighting that the return to baseline of
331 Ca^{2+} and TRPM4 current lags behind injected current ramp. C. Simulated somatic recordings in CCh (high
332 IP_3) with no nanodomain. C1. Voltage traces and current ramp. Note that more ramp current is required to
333 achieve the same firing rates as were achieved in B1. C2. Nanomolar Ca^{2+} concentration in outer shell
334 beneath the cell membrane. C3. No nanodomain. C4. There is negligible TRPM4 activation. In A2 and C2,
335 the red arrows point to when the $[Ca^{2+}]$ in the outer shell starts decreasing while the neuron keeps firing,
336 as opposed to B2.

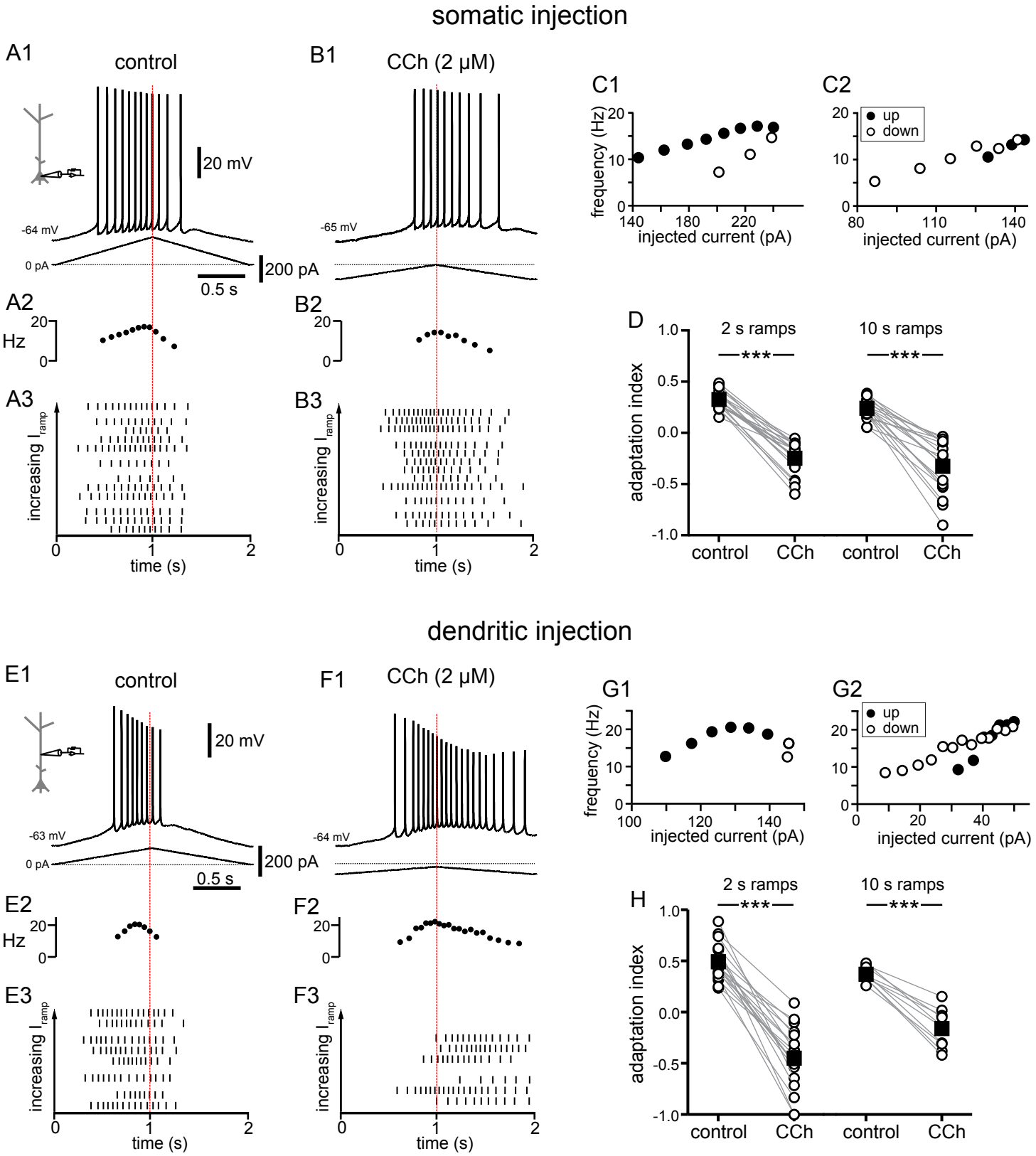
somatic injection
A1
control
20 mV
-64 mV
0 pA
200 pA
0.5 s
B1
CCh (2 μM)
-65 mV
C1
frequency (Hz)
injected current (pA)
C2
up
down
injected current (pA)
A2
Hz
B2
A3
increasing I_{ramp}
time (s)
B3
D
2 s ramps
10 s ramps
***
adaptation index
control
CCh
control
CCh
dendritic injection
E1
control
20 mV
-63 mV
0 pA
200 pA
0.5 s
F1
CCh (2 μM)
-64 mV
G1
frequency (Hz)
injected current (pA)
G2
up
down
injected current (pA)
E2
Hz
F2
E3
increasing I_{ramp}
time (s)
F3
H
2 s ramps
10 s ramps
***
adaptation index
control
CCh
control
CCh

Figure 1

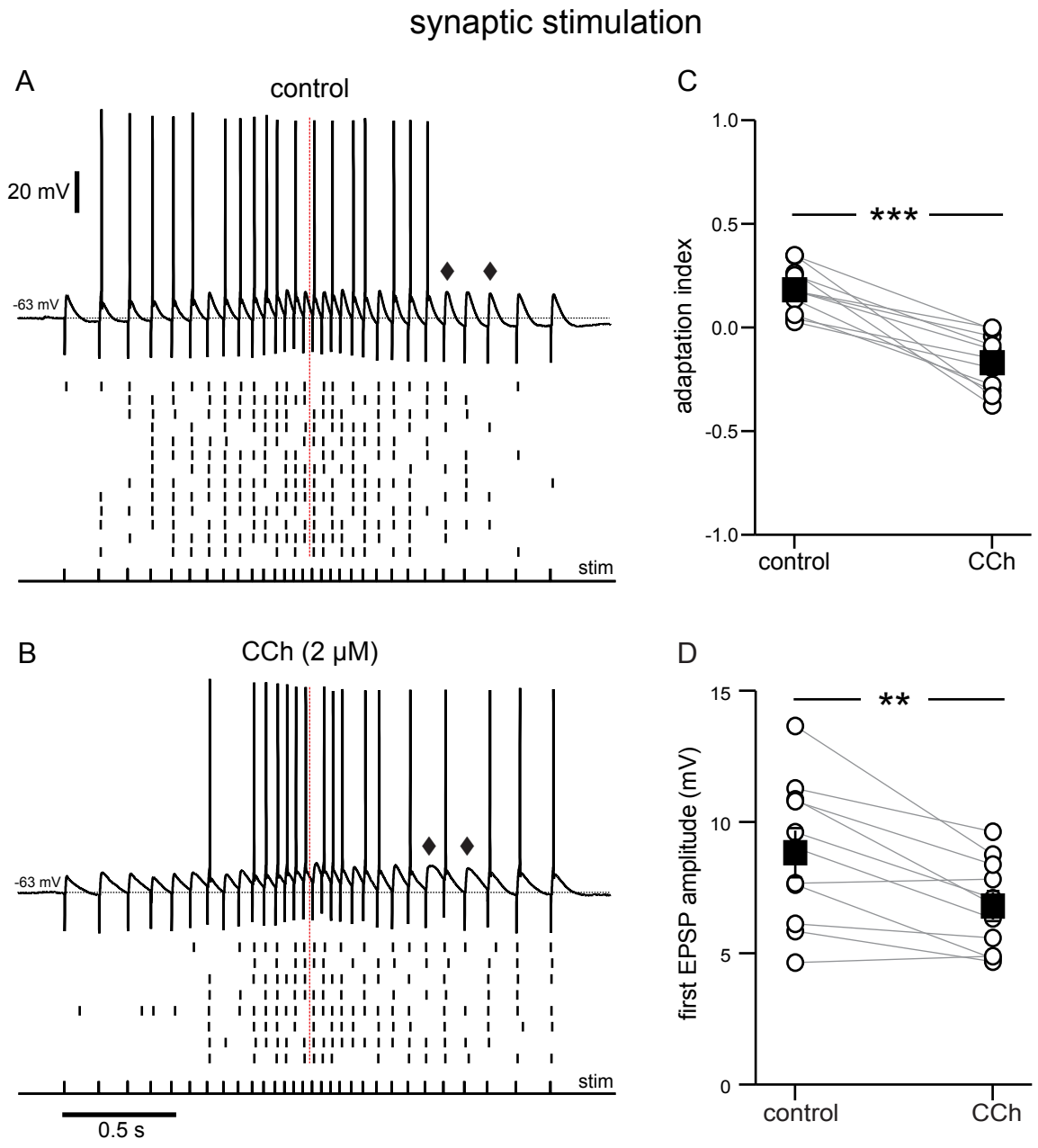
synaptic stimulation
A
control
20 mV
-63 mV
stim
B
CCh (2 μM)
-63 mV
stim
0.5 s
C
1.0
0.5
0.0
-0.5
-1.0
adaptation index
***
control
CCh
D
15
10
5
0
first EPSP amplitude (mV)
**
control
CCh

Figure 2

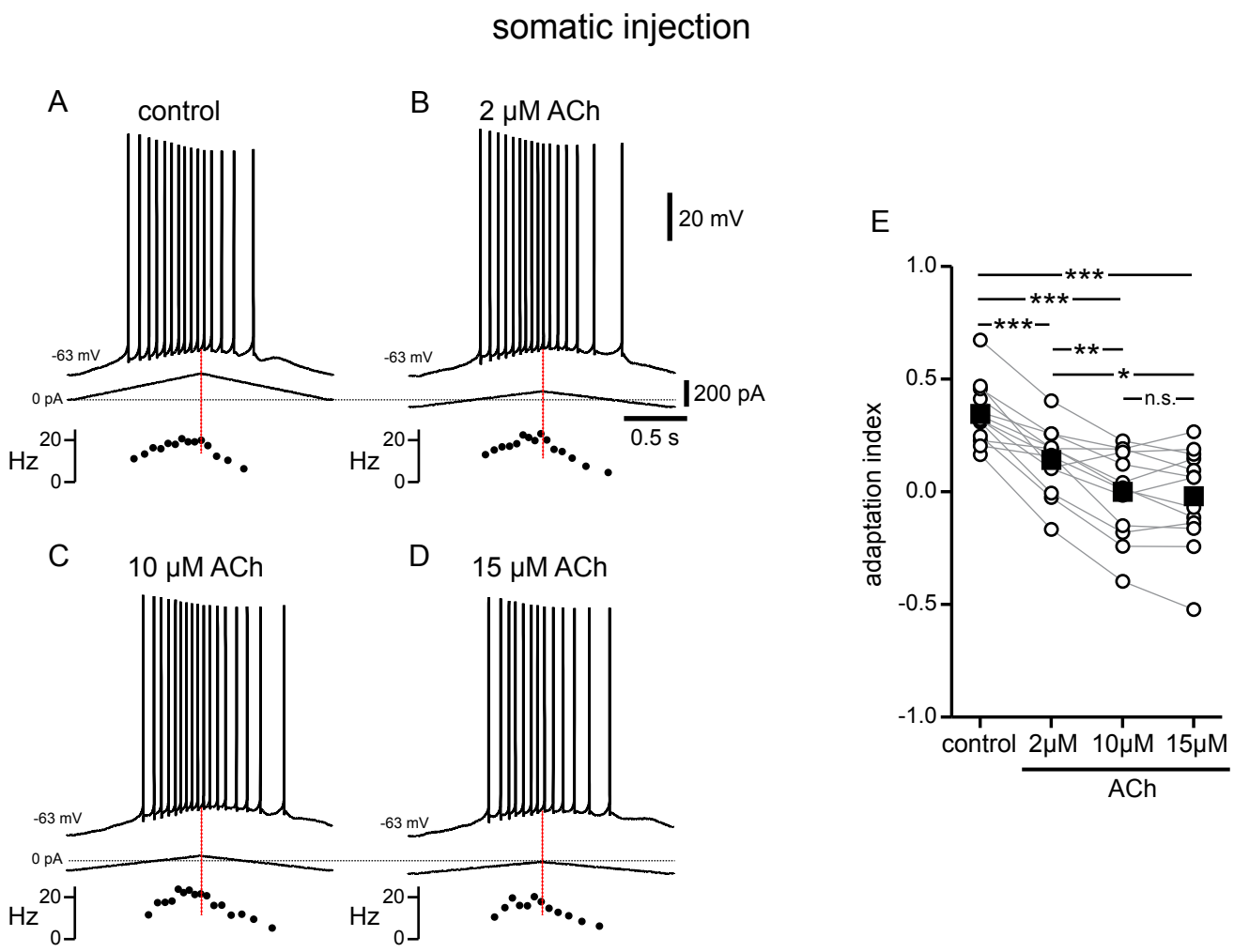
somatic injection
A
control
B
2 μM ACh
20 mV
-63 mV
0 pA
200 pA
0.5 s
Hz
20
0
C
10 μM ACh
D
15 μM ACh
E
adaptation index
1.0
0.5
0.0
-0.5
-1.0
***
***
***
**
*
n.s.
control
2μM
10μM
15μM
ACh

Figure 3

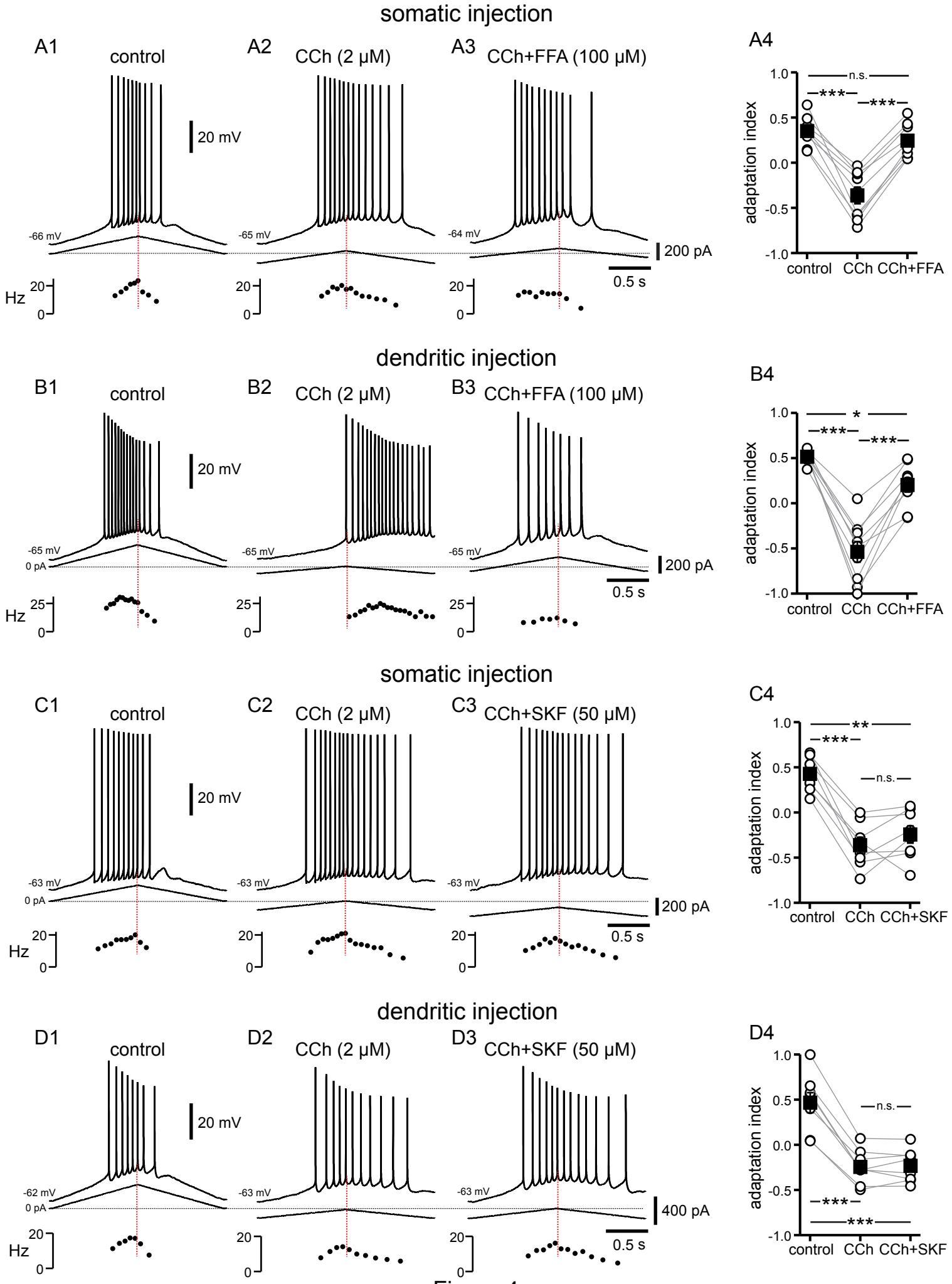
somatic injection
A1
control
A2
CCh (2 μM)
A3
CCh+FFA (100 μM)
A4
20 mV
-66 mV
-65 mV
-64 mV
200 pA
0.5 s
Hz
20
0
n.s.
***
***
adaptation index
1.0
0.5
0.0
-0.5
-1.0
control
CCh
CCh+FFA
dendritic injection
B1
control
B2
CCh (2 μM)
B3
CCh+FFA (100 μM)
B4
20 mV
-65 mV
0 pA
200 pA
0.5 s
Hz
25
0
*
***
***
adaptation index
control
CCh
CCh+FFA
somatic injection
C1
control
C2
CCh (2 μM)
C3
CCh+SKF (50 μM)
C4
20 mV
-63 mV
0 pA
200 pA
0.5 s
Hz
20
0
**
***
n.s.
adaptation index
control
CCh
CCh+SKF
dendritic injection
D1
control
D2
CCh (2 μM)
D3
CCh+SKF (50 μM)
D4
20 mV
-62 mV
-63 mV
0 pA
400 pA
0.5 s
Hz
20
0
n.s.
***
***
adaptation index
control
CCh
CCh+SKF

Figure 4

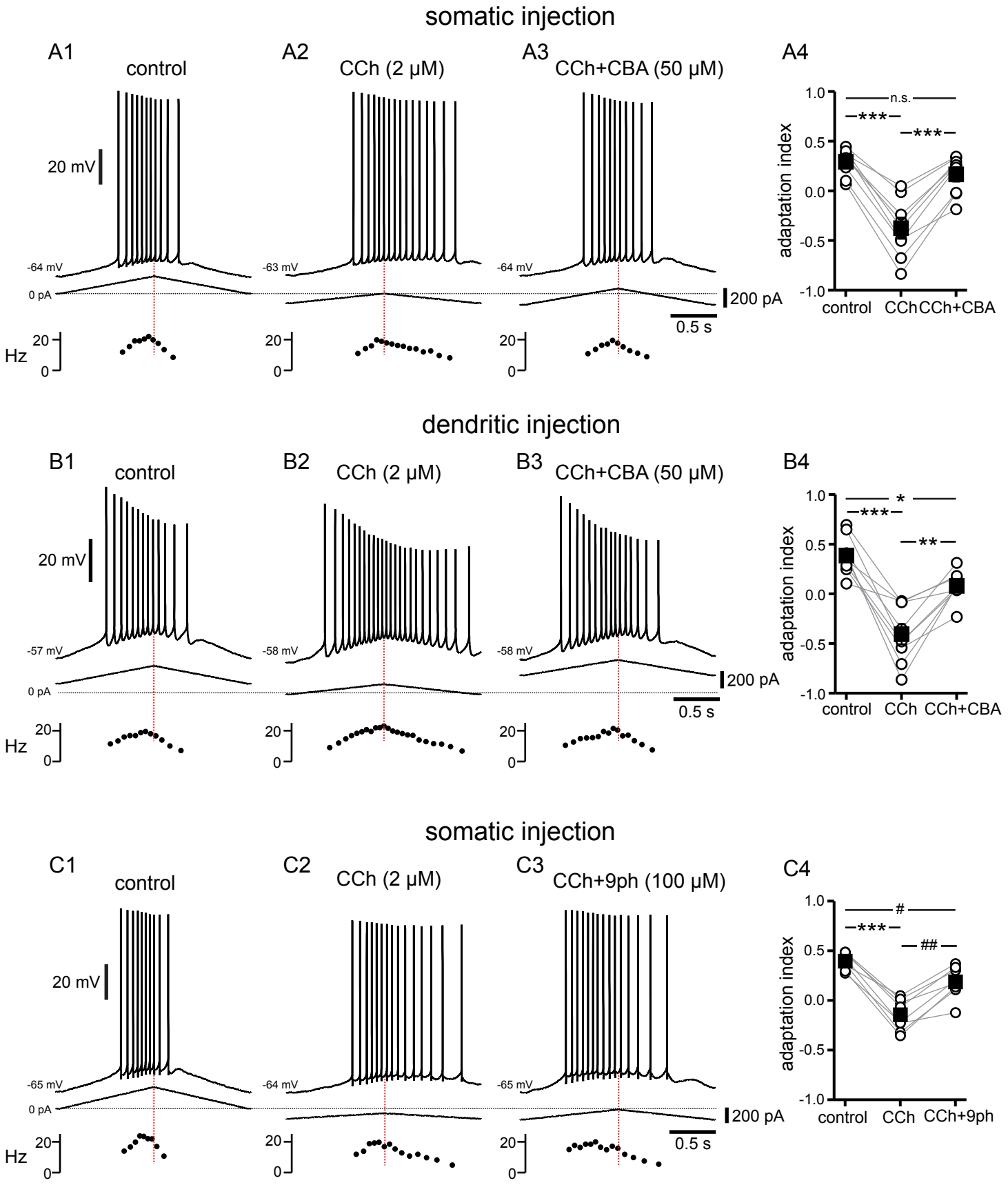
somatic injection
A1
control
A2
CCh (2 μM)
A3
CCh+CBA (50 μM)
A4
20 mV
-64 mV
-63 mV
-64 mV
0 pA
200 pA
0.5 s
Hz
20
0
adaptation index
1.0
0.5
0.0
-0.5
-1.0
n.s.
***
***
control
CCh
CCh+CBA
dendritic injection
B1
control
B2
CCh (2 μM)
B3
CCh+CBA (50 μM)
B4
20 mV
-57 mV
-58 mV
-58 mV
0 pA
200 pA
0.5 s
Hz
20
0
adaptation index
1.0
0.5
0.0
-0.5
-1.0
*
***
**
control
CCh
CCh+CBA
somatic injection
C1
control
C2
CCh (2 μM)
C3
CCh+9ph (100 μM)
C4
20 mV
-65 mV
-64 mV
-65 mV
0 pA
200 pA
0.5 s
Hz
20
0
adaptation index
1.0
0.5
0.0
-0.5
-1.0
#
***
##
control
CCh
CCh+9ph

Figure 5

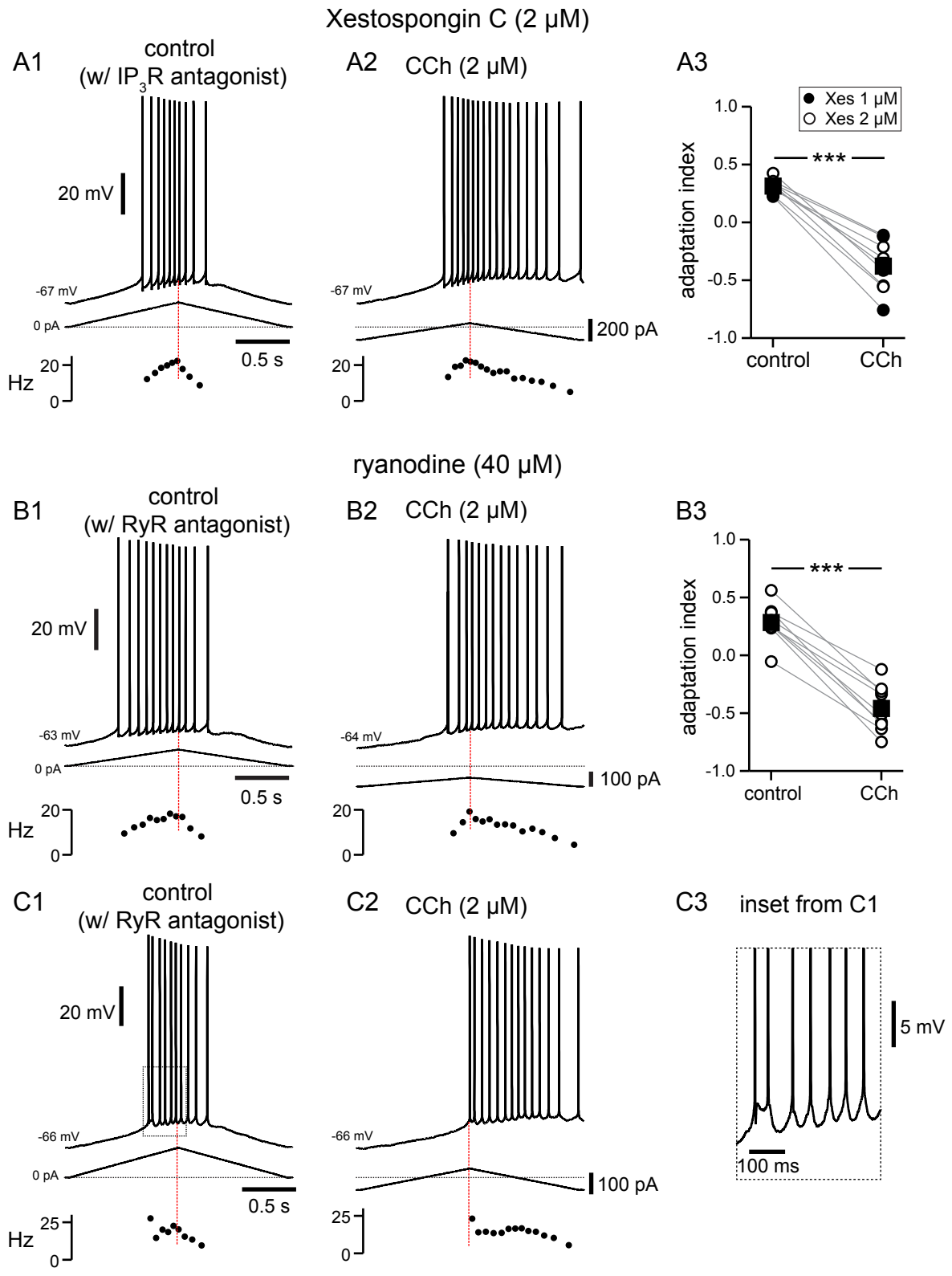
Xestospongin C (2 μM)
A1
control
(w/ IP3R antagonist)
20 mV
-67 mV
0 pA
0.5 s
Hz
20
0
A2
CCh (2 μM)
-67 mV
200 pA
20
0
A3
Xes 1 μM
Xes 2 μM
***
adaptation index
1.0
0.5
0.0
-0.5
-1.0
control
CCh
ryanodine (40 μM)
B1
control
(w/ RyR antagonist)
20 mV
-63 mV
0 pA
0.5 s
Hz
20
0
B2
CCh (2 μM)
-64 mV
100 pA
20
0
B3
***
adaptation index
1.0
0.5
0.0
-0.5
-1.0
control
CCh
C1
control
(w/ RyR antagonist)
20 mV
-66 mV
0 pA
0.5 s
Hz
25
0
C2
CCh (2 μM)
-66 mV
100 pA
25
0
C3
inset from C1
5 mV
100 ms

Figure 6

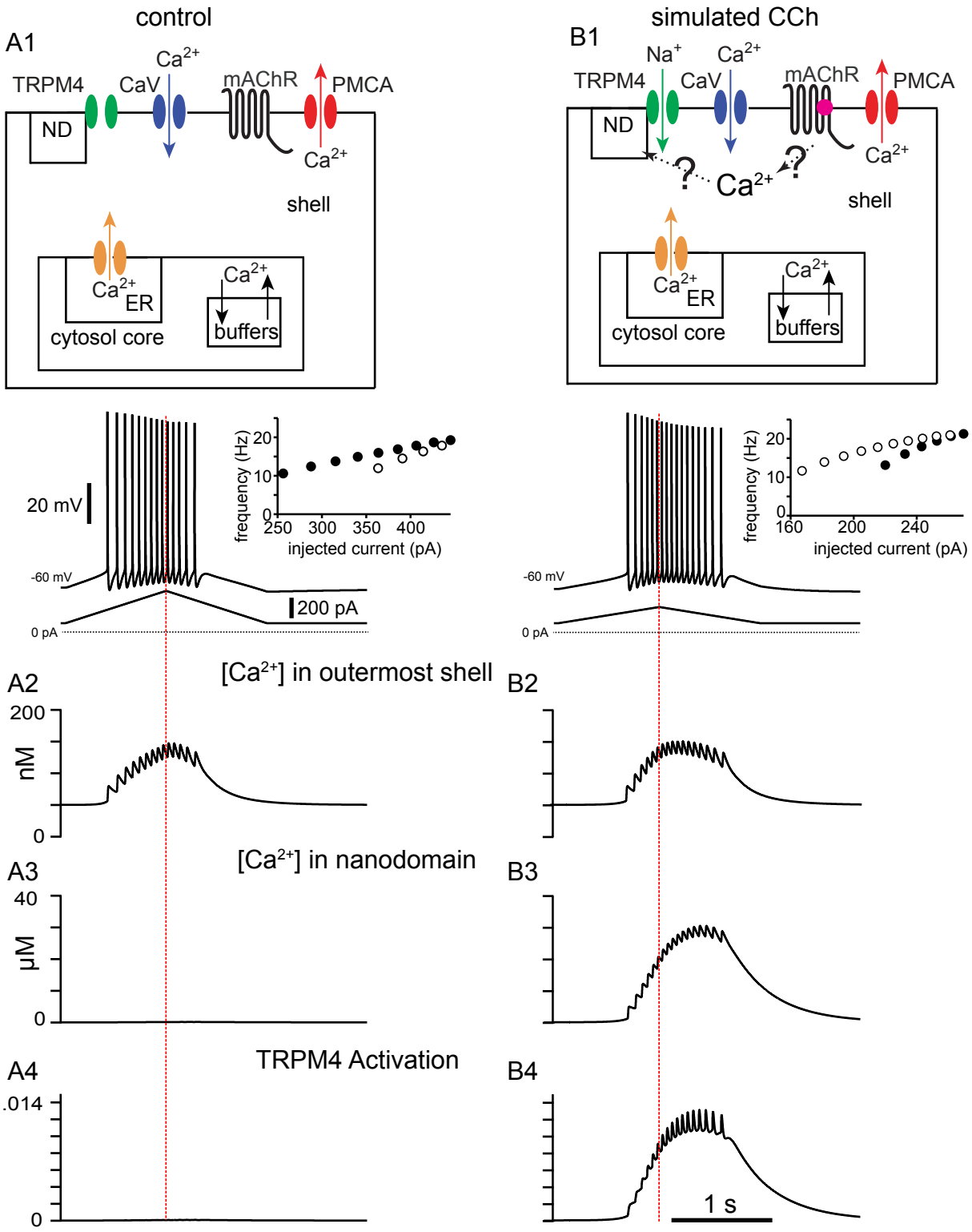
control
A1
TRPM4
CaV
Ca2+
mAChR
PMCA
ND
Ca2+
shell
Ca2+
ER
cytosol core
Ca2+
buffers
simulated CCh
B1
Na+
Ca2+
TRPM4
CaV
mAChR
PMCA
ND
?
Ca2+
?
Ca2+
shell
Ca2+
ER
cytosol core
Ca2+
buffers
20 mV
-60 mV
0 pA
200 pA
frequency (Hz)
injected current (pA)
[Ca2+] in outermost shell
A2
B2
200
nM
0
[Ca2+] in nanodomain
A3
B3
40
μM
0
TRPM4 Activation
A4
B4
.014
0
1 s

Figure 7

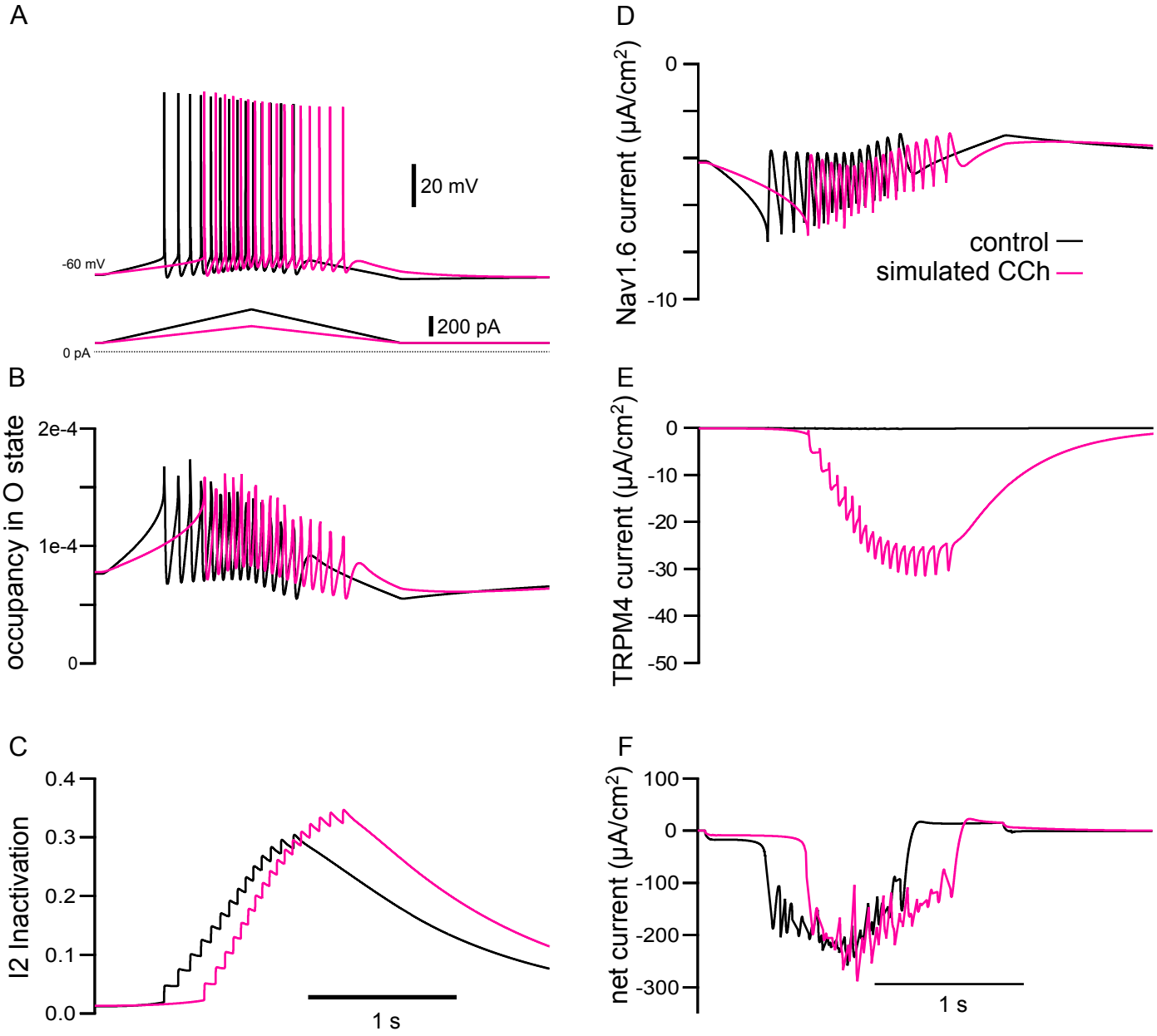
A
20 mV
-60 mV
200 pA
0 pA
B
occupancy in O state
2e-4
1e-4
0
C
I2 Inactivation
0.4
0.3
0.2
0.1
0.0
1 s
D
Nav1.6 current (μA/cm2)
0
-10
control
simulated CCh
E
TRPM4 current (μA/cm2)
0
-10
-20
-30
-40
-50
F
net current (μA/cm2)
100
0
-100
-200
-300
1 s

Figure 8

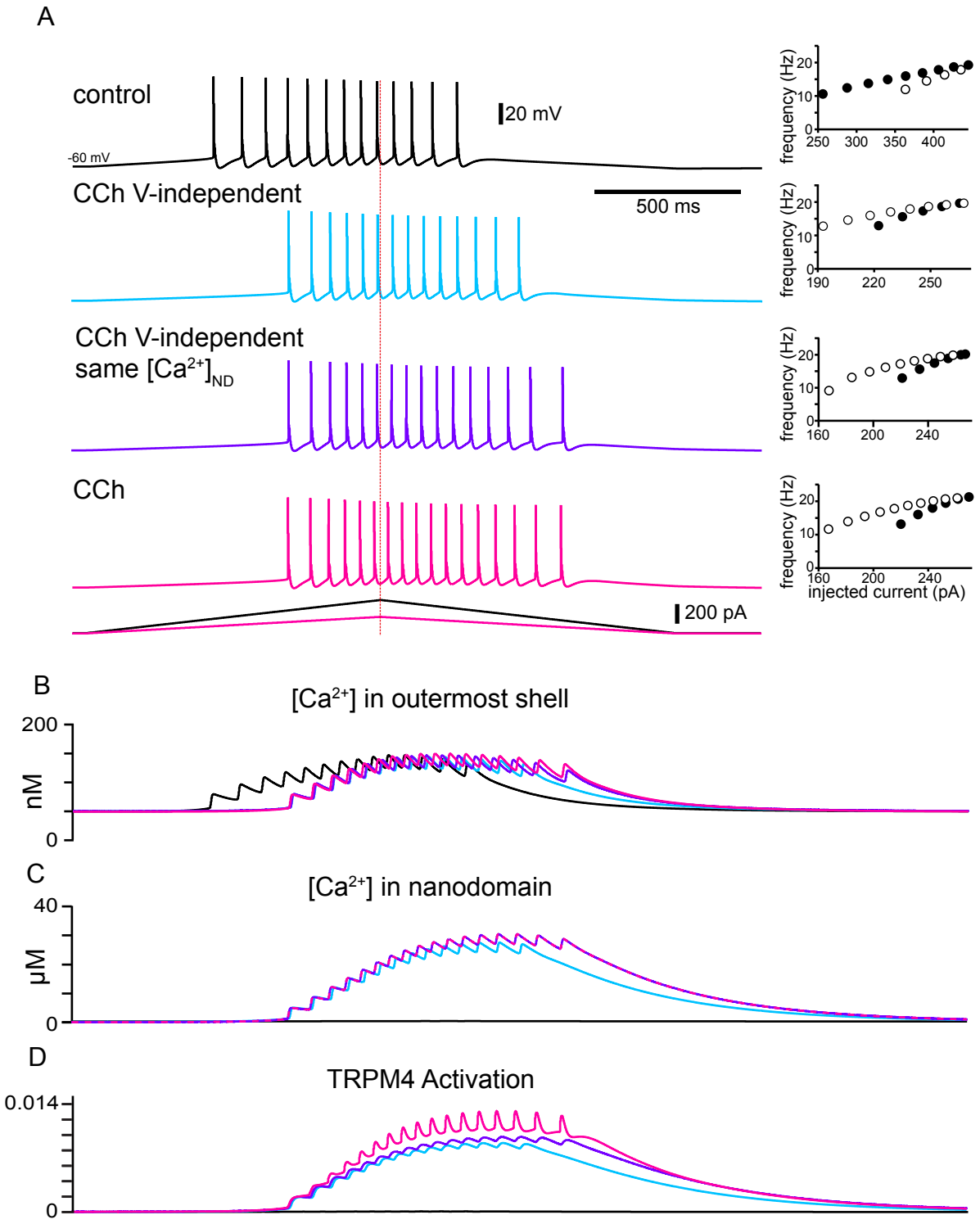
A
control
-60 mV
20 mV
500 ms
CCh V-independent
CCh V-independent
same [Ca2+]ND
CCh
200 pA
frequency (Hz)
injected current (pA)
B
[Ca2+] in outermost shell
200
nM
0
C
[Ca2+] in nanodomain
40
μM
0
D
TRPM4 Activation
0.014
0

Figure 9

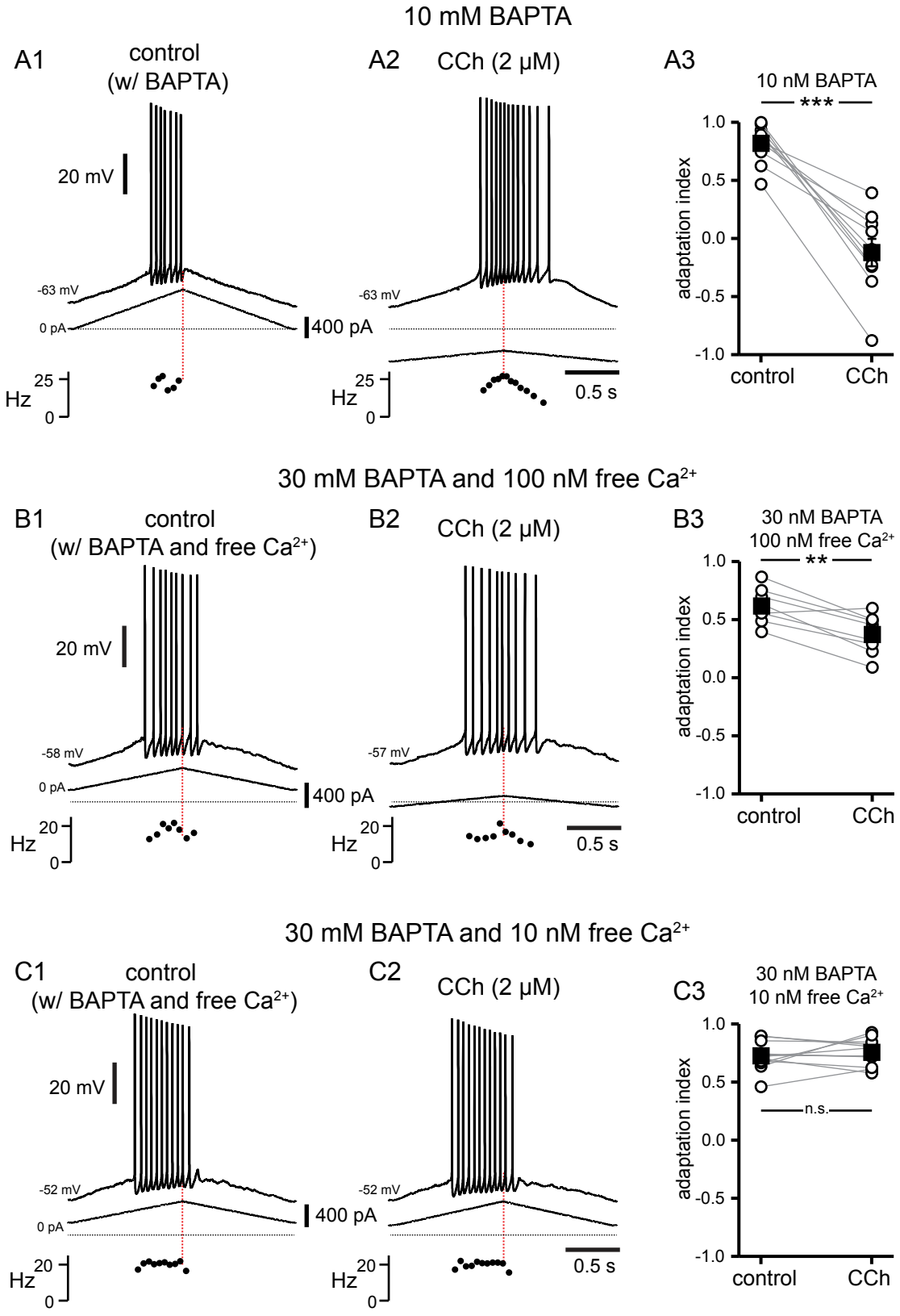
10 mM BAPTA
A1
control
(w/ BAPTA)
20 mV
-63 mV
0 pA
400 pA
Hz
25
0
A2
CCh (2 μM)
-63 mV
0.5 s
A3
10 nM BAPTA
***
adaptation index
1.0
0.5
0.0
-0.5
-1.0
control
CCh
30 mM BAPTA and 100 nM free Ca2+
B1
control
(w/ BAPTA and free Ca2+)
20 mV
-58 mV
0 pA
400 pA
Hz
20
0
B2
CCh (2 μM)
-57 mV
0.5 s
B3
30 nM BAPTA
100 nM free Ca2+
**
adaptation index
control
CCh
30 mM BAPTA and 10 nM free Ca2+
C1
control
(w/ BAPTA and free Ca2+)
20 mV
-52 mV
0 pA
400 pA
Hz
20
0
C2
CCh (2 μM)
-52 mV
0.5 s
C3
30 nM BAPTA
10 nM free Ca2+
n.s.
adaptation index
control
CCh

Figure 10

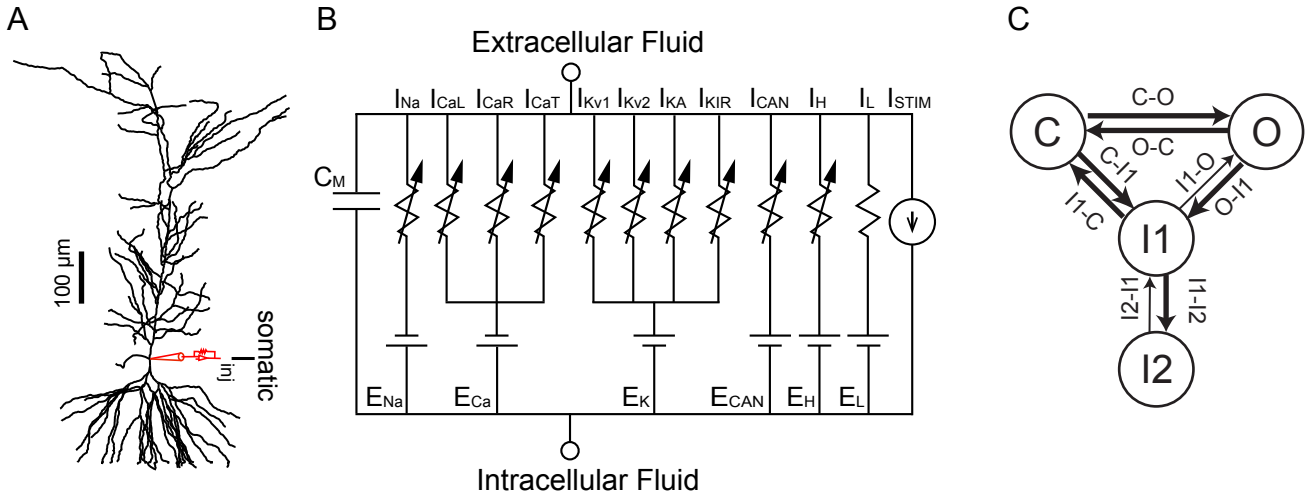
A
100 µm
somatic
inj
B
Extracellular Fluid
INa ICaL ICaR ICaT IKv1 IKv2 IKA IKIR ICAN IH IL ISTIM
CM
ENa ECa EK ECAN EH EL
Intracellular Fluid
C
C
O
I1
I2
C-O
O-C
C-I1
I1-C
I1-O
O-I1
I2-I1
I1-I2

Figure 11

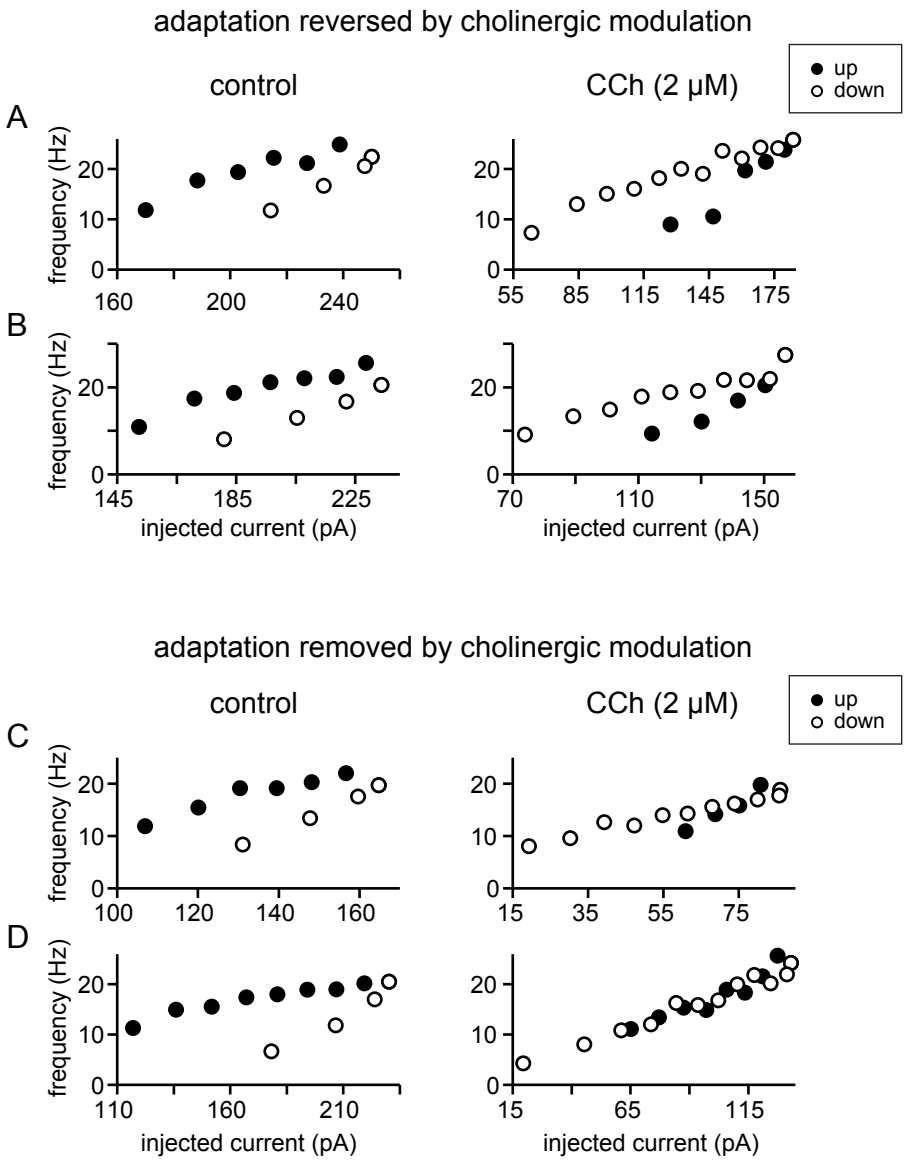

Figure 1 Supplement 1

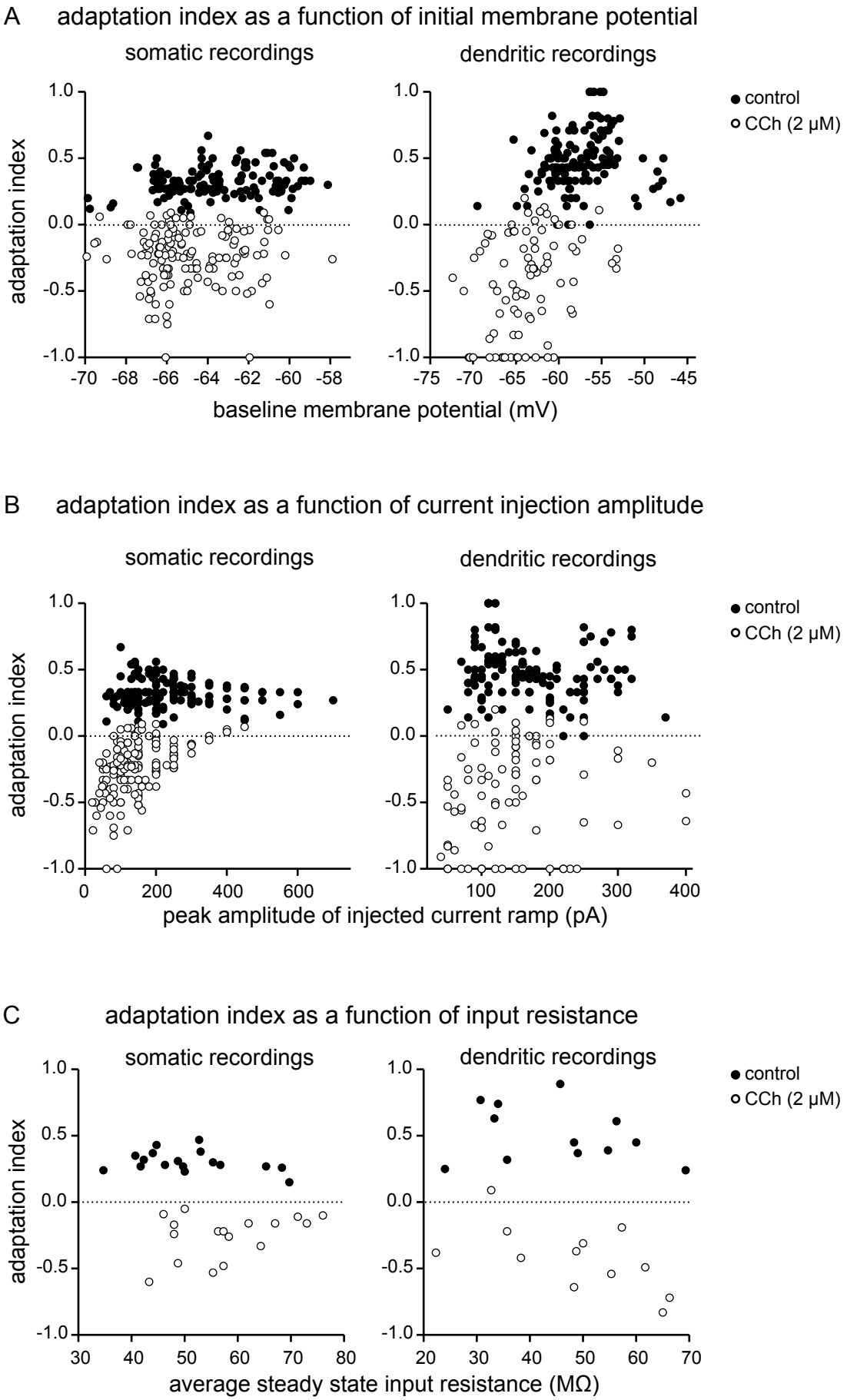

Figure 1 Supplement 2

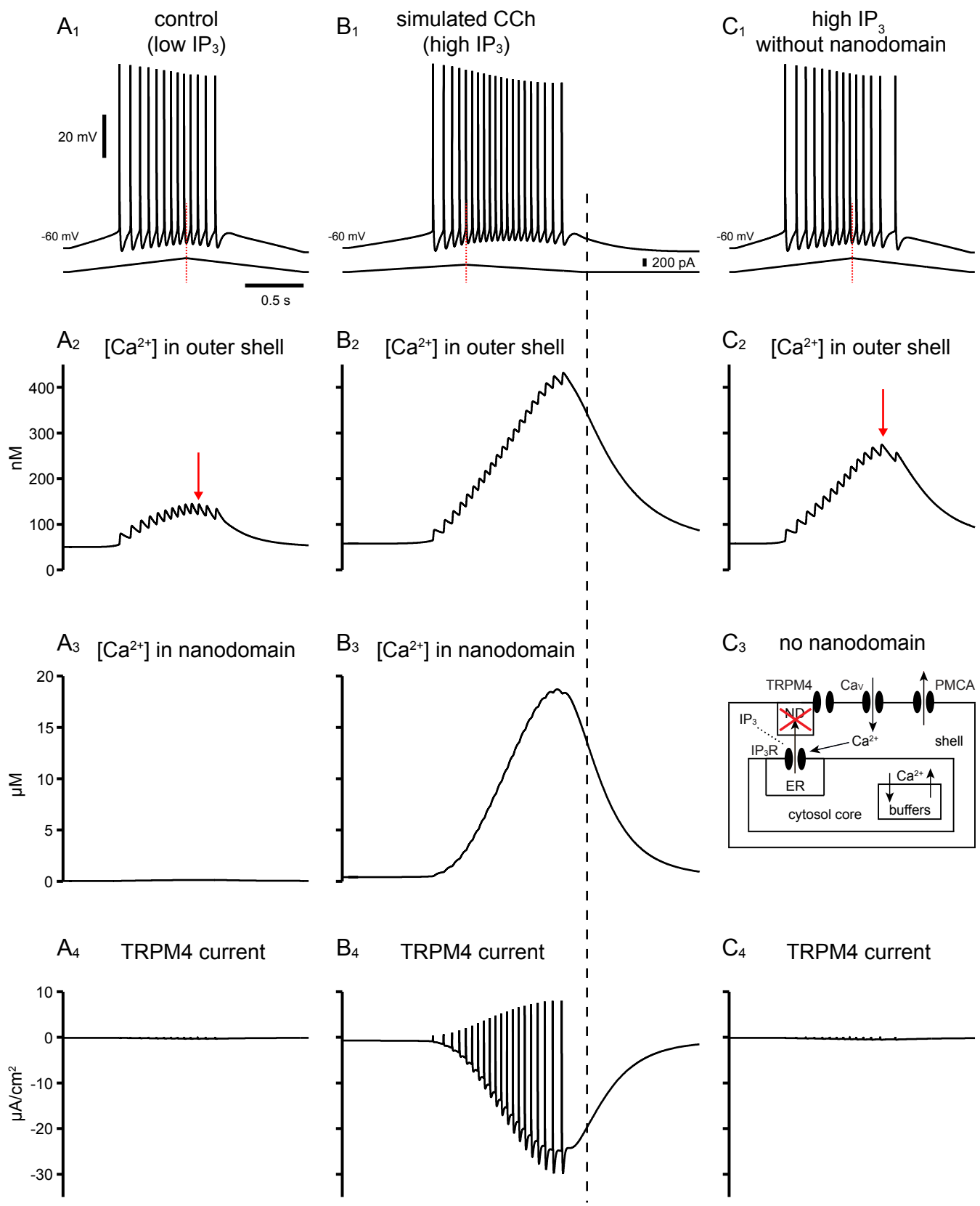

Figure 11 Supplement 1